



Auto-inhibition of Cnn binding to γ -TuRCs prevents ectopic microtubule nucleation and cell division defects

Corinne A Tovey, Chisato Tsuji, Alice Egerton, Fred Bernard, Antoine Guichet, Marc de La Roche, Paul Conduit

► To cite this version:

Corinne A Tovey, Chisato Tsuji, Alice Egerton, Fred Bernard, Antoine Guichet, et al.. Auto-inhibition of Cnn binding to γ -TuRCs prevents ectopic microtubule nucleation and cell division defects. *Journal of Cell Biology*, In press. hal-03218707

HAL Id: hal-03218707

<https://hal.science/hal-03218707>

Submitted on 5 May 2021

HAL is a multi-disciplinary open access archive for the deposit and dissemination of scientific research documents, whether they are published or not. The documents may come from teaching and research institutions in France or abroad, or from public or private research centers.

L'archive ouverte pluridisciplinaire **HAL**, est destinée au dépôt et à la diffusion de documents scientifiques de niveau recherche, publiés ou non, émanant des établissements d'enseignement et de recherche français ou étrangers, des laboratoires publics ou privés.

1 Auto-inhibition of Cnn binding to γ -TuRCs prevents ectopic microtubule nucleation 2 and cell division defects

•

5

3

5 Corinne A. Tovey^{1,2}, Chisato Tsuji¹, Alice Egerton¹, Fred Bernard², Antoine Guichet², Marc de
6 la Roche³, and Paul T. Conduit^{1, 2, 4}

7

⁸ ¹Department of Zoology, University of Cambridge, Downing Street, Cambridge, CB2 3EJ

9

10 ²Université de Paris, CNRS, Institut Jacques Monod, F75006, Paris, France.

11

12 ³Department of Biochemistry, University of Cambridge, 80 Tennis Court Road, Cambridge,
13 CB2 1GA, United Kingdom

14

15 ⁴Corresponding author

16 Paul T. Conduit

17 Institut Jacques Monod

18 CNRS - Université de Paris

19 15 rue Hélène Brion

20 75013 Paris

21 France

22 0033 (1) 57 27 80 95

23 paul.conduit

24 ORCID

25

26

5.0.0 Summary

27 We show that dste1 inhibition regulates the binding between microtubule nucleating complex
28 and proteins that tether them to sites of microtubule nucleation. Failure to regulate this binding
29 properly can lead to ectopic cytosolic microtubule nucleation and major defects during cell
30 division.

31

32 **Abstract**

33 γ -tubulin ring complexes (γ -TuRCs) nucleate microtubules. They are recruited to centrosomes
34 in dividing cells via binding to N-terminal CM1 domains within γ -TuRC-tethering proteins,
35 including *Drosophila* Centrosomin (Cnn). Binding promotes microtubule nucleation and is
36 restricted to centrosomes in dividing cells, but the mechanism regulating binding remains
37 unknown. Here we identify an extreme N-terminal “CM1 auto-inhibition” (CAI) domain found
38 specifically within the centrosomal isoform of Cnn (Cnn-C) that inhibits γ -TuRC binding.
39 Robust binding occurs after removal of the CAI domain or with the addition of phospho-mimetic
40 mutations, suggesting that phosphorylation helps relieve inhibition. We show that regulation
41 of Cnn binding to γ -TuRCs is isoform-specific and that mis-regulation of binding can result in
42 ectopic cytosolic microtubules and major defects during cell division. We also find that human
43 CDK5RAP2 is auto-inhibited from binding γ -TuRCs, suggesting conservation across species.
44 Overall, our results shed light on how and why CM1 domain binding to γ -TuRCs is regulated.

45 **Introduction**

46 Microtubules are organised into specialised arrays crucial for cell function, such as the mitotic
47 spindle. Correct array assembly relies in part on the spatiotemporal regulation of microtubule
48 formation, and this is achieved by restricting microtubule formation and organisation to
49 microtubule organising centres (MTOCs), such as the centrosome during mitosis (Tillery et
50 al., 2018; Sanchez and Feldman, 2016; Petry and Vale, 2015).

51

52 The common link between most MTOCs is the presence of multi-protein γ -tubulin ring
53 complexes (γ -TuRCs), which template and catalyse the kinetically unfavourable process of
54 microtubule nucleation (Kollman et al., 2011; Teixidó-Travesa et al., 2012; Lin et al., 2014a;
55 Tovey and Conduit, 2018; Farache et al., 2018). γ -TuRCs are recruited to MTOCs by γ -TuRC-
56 tethering proteins that directly link γ -TuRCs to the MTOC. γ -TuRCs contain 14 γ -tubulin
57 molecules held in a single-turn helical conformation by laterally associating γ -tubulin complex
58 proteins (GCPs). Each γ -tubulin molecule binds directly to an α/β -tubulin dimer to promote
59 new microtubule assembly. γ -TuRCs have a low activity within the cytosol but are thought to
60 be “activated” after recruitment to MTOCs. In this model, the controlled recruitment and
61 activation of γ -TuRCs enables the spatiotemporal control of microtubule nucleation and array
62 formation. Recent structural studies have shown that γ -TuRCs purified from the cytosol of
63 HeLa cells and *Xenopus* eggs are in a semi-open conformation, in which the γ -tubulin
64 molecules do not perfectly match the geometry of a 13 protofilament microtubule (Consolati
65 et al., 2020; Liu et al., 2019; Wieczorek et al., 2019). A conformational change into a fully
66 closed ring that matches microtubule geometry is expected to increase the nucleation capacity
67 of the γ -TuRC. This agrees with studies in budding yeast showing conformational differences
68 between γ -TuRC-like structures formed *in vitro* and γ -TuRCs bound to microtubules *in vivo*,
69 and where artificial “closure” of γ -TuRCs increases microtubule nucleation capacity (Kollman
70 et al., 2015).

71

72 How activation via an open-to-closed conformation change occurs is currently unclear, but
73 various factors have been reported to increase nucleation capacity. γ -TuRCs purified from
74 *Xenopus* egg extract nucleate much more efficiently after the addition of the TOG domain
75 protein XMAP215 (Thawani et al., 2020). TOG domain family members mediate α/β -tubulin
76 addition via their TOG domains (Nithianantham et al., 2018), bind directly to γ -tubulin, and
77 function in microtubule nucleation *in vitro* and *in vivo* (Wieczorek et al., 2015; Roostalu et al.,
78 2015; Thawani et al., 2018; Flor-Parra et al., 2018; Gunzelmann et al., 2018). Single molecule
79 experiments combined with modelling suggest that XMAP215 indirectly promotes the open-

80 to-closed conformation change of purified γ -TuRCs by increasing the chance of protofilament
81 formation, with lateral contacts between protofilaments promoting γ -TuRC closure (Thawani
82 et al., 2020). While an attractive model, evidence suggests that activation can occur in different
83 ways and may be context specific. Phosphorylation of γ -TuRCs by Aurora A around mitotic
84 chromatin increases γ -TuRC activity (Pinyol et al., 2013; Scrofani et al., 2015), as does
85 addition of NME7 kinase *in vitro* (Liu et al., 2014). γ -TuRC activity is also increased after
86 binding of the Augmin complex (Tariq et al., 2020), which tethers γ -TuRCs to other
87 microtubules.

88

89 Another well-documented potential γ -TuRC activator is the Centrosomin Motif 1 (CM1)
90 domain, which is conserved in γ -TuRC-tethering proteins across Eukaryotes (Sawin et al.,
91 2004; Zhang and Megraw, 2007; Lin et al., 2014b). Addition of protein fragments containing
92 the CM1 domain increase the nucleation capacity of γ -TuRCs purified from human cells (Choi
93 et al., 2010; Muroyama et al., 2016), although the degree of this activity change was much
94 lower or absent when using γ -TuRCs purified from *Xenopus* eggs (Liu et al., 2019; Thawani
95 et al., 2020). Expression of CM1 domain fragments within human cells leads to ectopic
96 cytosolic microtubule nucleation, and this is dependent on CM1 binding to γ -TuRCs (Choi et
97 al., 2010; Hanafusa et al., 2015; Cota et al., 2017). In fission yeast, expression of CM1 domain
98 fragments also results in cytosolic microtubule nucleation (Lynch et al., 2014), and in *Xenopus*
99 addition of CM1-domain fragments increases microtubule aster formation within egg extracts
100 supplemented with activated Ran (Liu et al., 2019). In budding yeast, CM1 domain binding
101 appears to move γ -tubulin molecules into a better position for nucleation (Brilot et al., 2021).
102 While large global structural changes were not observed in mammalian γ -TuRCs bound by
103 the CM1 domain (Liu et al., 2019; Wieczorek et al., 2019), local structural changes can be
104 observed, suggesting that more global changes could in theory occur with a higher
105 stoichiometry of binding (Brilot et al., 2021).

106

107 Given that CM1-domain binding leads to microtubule nucleation, binding is likely
108 spatiotemporally controlled, particularly during cell division. This idea is consistent with results
109 from numerous mass spectrometry experiments showing that γ -TuRCs do not readily
110 associate with CM1-domain proteins within the cytosol (Oegema et al., 1999; Choi et al., 2010;
111 Hutchins et al., 2010; Teixidó-Travesa et al., 2012; Thawani et al., 2018; Liu et al., 2019;
112 Wieczorek et al., 2019; Consolati et al., 2020). Binding of the human and *C. elegans* CM1
113 domain proteins, CDK5RAP2 and SPD-5, to γ -TuRCs involves phosphorylation (Hanafusa et
114 al., 2015; Ohta et al., 2021), which can be a means to spatiotemporally control binding.

115 Nevertheless, whether phosphorylation directly promotes binding to γ -TuRCs or regulates
116 binding in a different way remains unclear.

117

118 *Drosophila* Centrosomin (Cnn) is the only reported CM1-domain protein in *Drosophila* but is a
119 multi-isoform gene with all isoforms containing the CM1 domain (Eisman et al., 2009). The
120 centrosomal isoform (Cnn-C) has a dual role, both in recruiting γ -TuRCs to centrosomes
121 (Zhang and Megraw, 2007; Conduit et al., 2014b) and in forming a centrosome-scaffold that
122 supports mitotic pericentriolar material assembly (Conduit et al., 2014a; Feng et al., 2017).
123 Phosphorylation of a central Phospho-regulated multimerisation (PReM) domain specifically
124 at centrosomes promotes interactions between the PReM and C-terminal CM2 domains and
125 drives the oligomerisation of Cnn-C molecules into a scaffold-like structure that helps recruit
126 other centrosomal proteins (Conduit et al., 2014a; Feng et al., 2017). Testes-specific Cnn-T
127 isoforms have mitochondrial localisation domains instead of the PReM and CM2 domains and
128 recruits γ -TuRCs to mitochondria in sperm cells (Chen et al., 2017). Cnn-C and Cnn-T also
129 vary in their extreme N-terminal regions, upstream of the CM1 domain, with Cnn-C containing
130 a longer sequence.

131

132 Here, we show that the longer extreme N-terminal region of Cnn-C inhibits binding to γ -TuRCs
133 and therefore name this region the CM1 auto-inhibition (CAI) domain. Removal of the CAI
134 domain leads to robust binding, similar to that observed for the N-terminal region of Cnn-T.
135 We identify two putative phosphorylation sites, one in the CAI domain (T²⁷) and one
136 downstream of the CM1 domain (S¹⁸⁶), that promote binding to γ -TuRCs when phospho-
137 mimicked, suggesting that phosphorylation relieves CAI domain auto-inhibition. We show that
138 auto-inhibition is important, as expressing a form of Cnn that binds to cytosolic γ -TuRCs leads
139 to cytosolic microtubule nucleation and major defects during cell division. We further show
140 that human CDK5RAP2 is inhibited from binding γ -TuRCs in the cytosol by a region
141 downstream of the CM1 domain, showing that auto-inhibition of binding is a conserved feature
142 of CM1 domain proteins.

143 **Results**

144 **The extreme N-terminal region of Cnn-C is inhibitory for γ -TuRC binding**

145 We previously published evidence that different isoforms of Cnn bind γ -TuRCs with different
146 affinities (Tovey et al., 2018). We found that bacterially purified MBP-tagged N-terminal
147 fragments of Cnn-T (MBP-Cnn-T-N) could co-immunoprecipitate more cytosolic γ -tubulin than
148 the equivalent fragments of Cnn-C (MBP-Cnn-C-N). Both isoforms share a short sequence
149 just proximal to the CM1 domain (residues 78-97 in Cnn-C), but differ in their extreme N-
150 terminal region, which is 77 and 19 residues in Cnn-C and Cnn-T, respectively (Figure 1A).
151 We had hypothesised that the larger extreme N-terminal region of Cnn-C may auto-inhibit the
152 CM1 domain, restricting its ability to bind γ -TuRCs. To address this directly, and to confirm
153 the *in vitro* results, we developed an *in vivo* assay where γ -TuRC recruitment to different types
154 of Cnn “scaffolds” formed within eggs could be monitored. To form scaffolds within eggs we
155 injected *in vitro*-generated mRNA encoding Cnn-C with phospho-mimetic mutations within the
156 PReM domain (Cnn-C-PReM^m) (Figure 1B). The mRNA is translated into protein within the
157 egg and the phospho-mimetic mutations cause the Cnn molecules to oligomerise into
158 centrosome-like scaffolds throughout the cytosol (Conduit et al., 2014a) (Figure 1C-F; Figure
159 S1). To investigate how binding between Cnn and γ -TuRCs is regulated, we modified the N-
160 terminal region of Cnn-C-PReM^m (Figure 1B) and measured how efficiently fluorescently-
161 tagged γ -TuRC proteins could be recruited to the scaffolds.

162

163 We first compared the recruitment of endogenously tagged γ -tubulin37C-mCherry to GFP-
164 tagged scaffolds formed from unmodified Cnn-C-PReM^m with recruitment to scaffolds where
165 the extreme N-terminal region (dark blue in Figure 1A,B) was either exchanged with the
166 extreme N-terminal region of Cnn-T (red in Figure 1A,B) (Cnn-T-PReM^m) or was removed
167 (Cnn-C^{Δ1-77}-PReM^m). We also tested scaffolds in which all N-terminal amino acids up until the
168 start of the CM1 domain were removed (Cnn-C^{Δ1-97}-PReM^m). For simplicity we refer to these
169 as Cnn-C, Cnn-T, Cnn-C^{Δ1-77}, and Cnn-C^{Δ1-97} scaffolds, respectively, regardless of the
170 fluorescent tag used. Initial observations suggested that γ -tubulin associated much more
171 readily with Cnn-T and Cnn-C^{Δ1-77} scaffolds than with Cnn-C or Cnn-C^{Δ1-97} scaffolds (Figure
172 1C-F). This was clear after plotting the GFP (Cnn) and mCherry (γ -tubulin) fluorescence
173 values for individual scaffolds from multiple embryos per condition (Figure 1G). To quantify γ -
174 tubulin recruitment we performed linear regression for each egg separately and plotted the
175 slope of these lines (S values, in arbitrary units). The mean S value provides an estimate for
176 the relative binding affinity between the different forms of Cnn and γ -tubulin complexes (Figure
177 1H). The mean S values for Cnn-T scaffolds (7.81) and Cnn-C^{Δ1-77} scaffolds (5.01) were ~13-

178 fold and 9-fold higher, respectively, than the mean S value for Cnn-C scaffolds (0.57).
179 Consistent with this, MBP-tagged N-terminal fragments of Cnn-T (MBP-Cnn-T-N) and Cnn-
180 C^{Δ1-77} (MBP-Cnn-C-N^{Δ1-77}) both co-immunoprecipitated more γ-tubulin from embryo extracts
181 than N-terminal fragments of Cnn-C (MBP-Cnn-C-N) (Figure 1I,J). Thus, the extreme N-
182 terminal region of Cnn-C (blue in Figure 1A,B) is inhibitory for binding to γ-tubulin complexes.
183

184 The ability of Cnn-C^{Δ1-77} to bind γ-tubulin complexes appeared to be dependent on the amino
185 acids just upstream of the CM1 domain (aa78-97), which are shared with Cnn-T (Figure 1A),
186 as the mean S value for Cnn-C^{Δ1-97} scaffolds (0.36) was not significantly different from the
187 mean S value for Cnn-C scaffolds (0.57) (Figure 1H). This is consistent with recent
188 observations in *S. cerevisiae*, showing that the equivalent amino acids within SPC110 make
189 close contacts with SPC98^{GCP3} (Brilot et al., 2021).

190
191 Cnn-T and Cnn-C^{Δ1-77} scaffolds also recruited the γ-TuRC-specific component Grip75^{GCP4}
192 better than Cnn-C scaffolds (Figure 2A-E). Similar to the recruitment of γ-tubulin, the mean S
193 values for Cnn-T (3.8) and Cnn-C^{Δ1-77} (3.1) scaffolds were 10.3-fold and 8.4-fold higher,
194 respectively, than the S value for Cnn-C (0.37) scaffolds (Figure 2E) (note that these S values
195 cannot be compared directly to those obtained from analysing γ-tubulin recruitment due to the
196 different fluorescent tags used). Moreover, a combination of western blotting and mass
197 spectrometry showed that bacterially purified MBP-Cnn-T-N fragments could co-
198 immunoprecipitate numerous other γ-TuRC components (Figure S2).

199
200 The data collectively show that the extreme N-terminal region of Cnn-C (aa1-77) inhibits
201 binding to γ-TuRCs. We therefore name this region the “CM1 auto-inhibition” (CAI) domain.
202

203 **γ-TuRCs recruited by Cnn scaffolds appear to be functional and can generate dynamic 204 microtubules**

205 We next compared the ability of different scaffold types to organise microtubules. We imaged
206 GFP-tagged Cnn-C (low γ-TuRC binding), Cnn-T, or Cnn-C^{Δ1-77} (high γ-TuRC binding)
207 scaffolds within eggs expressing the microtubule binding protein Jupiter-mCherry (Figure 3A-
208 C) and performed a blind analysis to categorise eggs into those containing scaffolds that
209 organised strong, weak, or no microtubule asters (Figure 3D). We also included a “tubulin
210 overlay” category, where the Jupiter-mCherry signal did not extend beyond the GFP scaffold
211 signal. The results show that Cnn-T and Cnn-C^{Δ1-77} scaffolds were much more likely to
212 organise microtubule asters than Cnn-C scaffolds (Figure 3D). This correlates with the

increased recruitment of γ -TuRCs to Cnn-T and Cnn-C $^{\Delta 1-77}$ scaffolds (Figure 1H), suggesting that these γ -TuRCs are able to nucleate microtubules. While it is possible that some microtubules could have been generated independently of γ -TuRCs, a process that occurs by tubulin concentration at *C. elegans* SPD-5 condensates formed *in vitro* (Woodruff et al., 2017), the increased microtubule organising capacity at Cnn-T and Cnn-C $^{\Delta 1-77}$ scaffolds (high γ -TuRC recruitment) compared to at Cnn-C scaffolds (low γ -TuRC recruitment) suggests that γ -TuRC-mediated microtubule nucleation/organisation is the predominant factor at these Cnn scaffolds.

221

Filming Cnn-T scaffolds through time revealed that the scaffolds could merge and could also be quite mobile, especially those that had microtubules emanating from just one side (Video 1). We could also observe events where spindle-like structures formed between adjacent Cnn-T or Cnn-C $^{\Delta 1-77}$ scaffolds (Figure 3E,F; Video 2 and 3), suggesting that the microtubules are dynamic and can be regulated by motor proteins. Giant Cnn-T scaffolds that rotated dragged their attached microtubules through the cytosol, indicating that the microtubules were robustly anchored to the scaffolds (Video 4). In summary, Cnn-T and Cnn-C $^{\Delta 1-77}$ scaffolds can recruit γ -TuRCs that are capable of nucleating and anchoring microtubules.

230

231 **Phospho-mimetic mutations help relieve CAI domain mediated auto-inhibition**

How could CAI domain mediated auto-inhibition be relieved to allow efficient binding to γ -TuRCs at centrosomes? Studies in human cells, *C. elegans*, and *S. cerevisiae* have shown that binding of CM1 domain proteins to γ -TuSCs or γ -TuRCs is promoted by phosphorylation close to the CM1 domain (Hanafusa et al., 2015; Ohta et al., 2021; Lin et al., 2014b) (Figure S3B). Moreover, Cnn-C binds γ -TuRCs and is phosphorylated only at centrosomes (Zhang and Megraw, 2007; Conduit et al., 2014b; a), suggesting a possible link between binding and phosphorylation.

239

In an attempt to find phosphorylation sites that may relieve CAI domain inhibition, we aligned amino acids 1 to ~255 of Cnn-C homologues from various *Drosophila* species. We identified three putative phosphorylation “patches” (P1, P2, P3) based on a high concentration of conserved serine and threonine residues (Figure 4A; Figure S3). P1 represented the only region within the CAI domain with predicted secondary structure, corresponding to an α -helix (Figure S3). We compared the amount of γ -tubulin that co-IP'd with purified MBP-tagged N-terminal fragments of Cnn-C containing phospho-mimetic mutations (S>D or T>E) in all serine and threonine residues within either P1 (MBP-Cnn-C-N P1), P2 (MBP-Cnn-C-N P2), P3 (MBP-

248 Cnn-C-N^{P3}), or in all three patches (MBP-Cnn-C-N^{P1-3}). The original MBP-Cnn-C-N (low
249 binding) and MBP-Cnn-T-N (high binding) fragments were included as negative and positive
250 controls, respectively. Of these phospho-mimetic fragments, MBP-Cnn-C-N^{P1} co-IP'd γ -tubulin
251 most efficiently, although not as efficiently as MBP-Cnn-T-N (Figure 4B,D). We therefore
252 generated phospho-mimetic fragments where either the proximal (S²¹, S²², T²⁷) or distal (T³¹,
253 T³³, S³⁴) three residues within P1 were mimicked (MBP-Cnn-C-N^{P1a} or MBP-Cnn-C-N^{P1b},
254 respectively). We also phospho-mimicked T²⁷ alone (MBP-Cnn-C-N^{T27}), because T²⁷ is a
255 putative Polo/Plk1 site and because a previous study reported centrosome defects when this
256 site was mutated to alanine *in vivo* (Eisman et al., 2015). MBP-Cnn-C-N^{P1a} and MBP-Cnn-C-
257 N^{T27}, but not MBP-Cnn-C-N^{P1b}, co-IP'd more γ -tubulin than MBP-Cnn-C-N, although again not
258 as much as MBP-Cnn-T-N (Figure 4C,D). In the scaffold assay, phospho-mimicking T²⁷ also
259 had a positive effect that was not as strong as that seen with Cnn-T or Cnn-C ^{Δ 1-77} scaffolds.
260 The mean S value for Cnn-C^{T27} scaffolds (1.35) was ~2.4-fold higher than for Cnn-C scaffolds
261 (0.57) but still lower than the S values for Cnn-T or Cnn-C ^{Δ 1-77} scaffolds (Figure 4G; note that
262 S values for Cnn-C^{T27E} scaffolds, and subsequent scaffolds analysed below, were compared
263 to the S values for Cnn-C, Cnn-T and Cnn-C ^{Δ 1-77} scaffolds from Figure 1H). Together, this
264 suggested that while phosphorylation of T²⁷ may be involved in relieving CAI domain auto-
265 inhibition (or in directly increasing the binding affinity between Cnn-C and γ -TuRCs), it is not
266 sufficient for robust γ -TuRC binding.

267
268 We therefore considered other putative phosphorylation sites. Phosphorylation slightly
269 downstream of the CM1 domain promotes binding to γ -TuRCs in humans and *C. elegans* CM1
270 domain proteins (Ohta et al., 2021; Hanafusa et al., 2015). While the sequence surrounding
271 the CM1 domain is not conserved across diverse species (Figure S3B), we identified two
272 serine residues (S173 and S186) downstream of the CM1 domain in Cnn that were conserved
273 in *Drosophila* species (Figure S3A). These sites also mapped to a similar predicted coiled-coil
274 region to the sites in human CDK5RAP2 and *C. elegans* SPD-5 (Figure S3B). While phospho-
275 mimicking S¹⁷³ had no effect, scaffolds with a phospho-mimetic mutation at S¹⁸⁶ (Cnn-CS186D
276 scaffolds) recruited ~3.8-fold more γ -tubulin than Cnn-C scaffolds (Figure 4G). Moreover, N-
277 terminal fragments containing this mutation (Cnn-C-NS¹⁸⁶) co-IP'd γ -tubulin with a similar, if
278 not higher, efficiency compared to the Cnn-T-N or Cnn-C ^{Δ 1-77} fragments (Figure 4E). In
279 addition, although not apparent in the scaffold assay (Figure 4G), phospho-mimicking both T²⁷
280 and S¹⁸⁶ had a synergistic effect in the co-IP assay, where Cnn-C-N^{T27,S186} fragments co-IP'd
281 significantly more γ -tubulin than any other type of fragment (Figure 4F). The same pattern was
282 seen when co-immunoprecipitating the γ -TuRC-specific protein Grip75^{GCP4}-sfGFP (Figure

283 4E). Unexpectedly, unlike in the co-IP assay, we did not see increased recruitment of
284 Grip^{75GCP4}-sfGFP to scaffolds containing any of the N-terminal phospho-mimetic mutations,
285 including Cnn-C^{T27,S186} scaffolds (Figure 4H). This suggested that these scaffolds recruit γ -
286 TuSCs rather than γ -TuRCs, potentially explaining why they do not recruit γ -tubulin to the
287 levels seen at Cnn-T or Cnn-C ^{Δ 1-77} scaffolds (Figure 4G). Nevertheless, Cnn-C^{T27,S168D}
288 scaffolds did organise microtubules more readily than Cnn-C scaffolds (Figure 4I – data
289 compared to that in Figure 3D), suggesting that the γ -tubulin complexes bound by the
290 phospho-mimetic forms of Cnn-C are at least semi-functional. Thus, while there are some
291 differences between the scaffold assay and the co-IP assay, the data collectively suggest that
292 phosphorylation at T²⁷ and in particular at S^{186D} help to relieve CAI domain auto-inhibition and
293 promote the binding of Cnn-C to γ -TuRCs.

294

295 **Ubiquitous expression of Cnn-C containing the high binding-affinity Cnn-T N-terminal
296 region has a dominant negative effect and leads to fertility defects**

297 We next tested whether Cnn-C auto-inhibition is important for cell and developmental fidelity
298 in *Drosophila*. We generated a transgenic fly line by random insertion of a ubiquitously-driven
299 untagged Cnn-C construct in which its N-terminal region had been replaced with the N-
300 terminal region of Cnn-T (pUbq-Cnn-C^T) (Figure 5A). Based on our data so far, this form of
301 Cnn should bind strongly to cytosolic γ -TuRCs but otherwise be regulated normally. We also
302 generated a control line ubiquitously expressing untagged wild-type Cnn-C (pUbq-Cnn-C),
303 whose binding to cytosolic γ -TuRCs should be restricted by the CAI domain.

304

305 It was difficult to generate a viable pUbq-Cnn-C^T line and, once generated, it was difficult to
306 maintain and combine with other alleles. Thus, all following experiments were performed with
307 the pUbq constructs expressed in the presence of endogenous Cnn. By crossing pUbq-Cnn-
308 C and pUbq-Cnn-C^T females or males to wild-type flies and quantifying embryo hatching rates,
309 we found that pUbq-Cnn-C^T flies were less able to generate progeny than pUbq-Cnn-C flies,
310 with males being more affected than females (Figure 5B). Western blots of embryo or testes
311 extracts using different Cnn-C antibodies and a Cnn-T-specific antibody showed that the level
312 of pUbq-Cnn-C^T (red arrowheads) relative to endogenous Cnn-C (black arrowheads) was
313 higher in testes extracts compared to embryo extracts (Figure 5C). In the embryo extracts, the
314 pUbq-Cnn-C^T band was much weaker than the endogenous Cnn-C band, which is unusual for
315 pUbq-driven Cnn constructs (P. Conduit unpublished observations), suggesting its expression
316 was being suppressed. In contrast, the pUbq-Cnn-C^T band was of a similar intensity to, if not
317 higher than, the endogenous Cnn-C band in the testes extracts. We therefore conclude that,

318 relative to endogenous Cnn-C, pUbq-Cnn-CT is weakly expressed within the maternal
319 germline but is expressed to levels similar to endogenous Cnn within the testes. While other
320 factors could be involved, such as cell-specific effects of Cnn to γ -TuRC binding, these
321 differences in the expression levels of pUbq-Cnn-CT between cells could explain the difference
322 in the ability of male and female flies to generate progeny.

323

324 **Mis-regulation of binding to γ -tubulin complexes results in ectopic microtubule
325 nucleation and defects during cell division**

326 The failure of pUbq-Cnn-CT flies to generate normal numbers of progeny suggested that
327 ectopic binding of Cnn to γ -TuRCs leads to cellular defects during germline or early
328 development. Co-IPs from embryo extracts confirmed that pUbq-Cnn-CT binds γ -TuRCs more
329 efficiently than pUbq-Cnn-C (Figure 5D). We immunostained female and male germline
330 tissues to investigate any potential defects within their cells. There were no obvious defects
331 within oocytes from pUbq-Cnn-CT females, where the positions of the nucleus and Gurken
332 protein, both dependent on proper microtubule organisation, were normal in oocytes from both
333 pUbq-Cnn-C and pUbq-Cnn-CT females (Figure S4A-C). We did, however, frequently observe
334 defects in fixed and stained syncytial embryos from pUbq-Cnn-CT females (Figure 6D-F) as
335 compared to embryos from pUbq-Cnn-C females (Figure 6A-C). These defects included: an
336 apparent excess of cytosolic microtubules, unusually bright microtubule asters, and nuclear
337 organisation defects during S-phase (Figure 6D); highly disorganised spindles during M-phase
338 (Figure 6E); and an apparent excess of cytosolic microtubules during telophase (Figure 6F).
339 In a blind analysis of embryos, severe and moderate defects were observed in a higher
340 proportion of embryos from pUbq-Cnn-CT females (19.4% severe and 30.6% moderate) than
341 from wild-type (4.1% and 18.4%) or pUbq-Cnn-C (3.4% and 25%) females (Figure 6G).
342 Broadly, the categorisation of embryo defects in Figure 6G reflects the observed hatching
343 rates in Figure 5B, assuming that embryos with moderate and severe defects often fail in
344 development. While half of the embryos from pUbq-Cnn-CT females were normal, this could
345 reflect the relatively low expression of pUbq-Cnn-CT in the female germline (Figure 5C).

346

347 To directly test whether binding of Cnn to cytosolic γ -TuRCs could promote ectopic
348 microtubule nucleation within embryos, we injected unfertilised eggs injected with mRNA
349 encoding GFP-Cnn-T-N, which efficiently binds cytosolic γ -TuRCs. We found that 9/12 of
350 these eggs displayed dynamic microtubules throughout their cytosol (Figure 6H; Video 5). This
351 was not observed in all 27 control-injected eggs. This effect is similar to that observed when
352 expressing CM1-domain fragments within human and fission yeast cells (Choi et al., 2010;

353 Cota et al., 2017; Hanafusa et al., 2015; Lynch et al., 2014) and suggests that CM1 domain
354 binding to γ -TuRCs also promotes microtubule nucleation in *Drosophila*.

355

356 Consistent with a very strong reduction in the ability of pUbq-Cnn-C^T males to generate
357 progeny, defects were frequently observed within their testes, where production of sperm
358 involves a series of mitotic and meiotic cell divisions. When meiosis progresses normally, the
359 64 round spermatids cells within the resulting cyst all contain a similarly sized phase-light
360 nucleus and phase-dark nebenkern (which is an accumulation of mitochondria that were
361 segregated during meiosis). This was true in round spermatids from pUbq-Cnn-C testes
362 (Figure 7A,C), but not in round spermatids from pUbq-Cnn-C^T testes (Figure 7B,C),
363 suggesting that pUbq-Cnn-C^T expression results in problems in chromosome segregation and
364 cytokinesis. Indeed, a high density of cytosolic microtubules and clear meiotic defects were
365 observed in spermatocytes within fixed and stained pUbq-Cnn-C^T, but not pUbq-Cnn-C,
366 testes. Defects were observed at various developmental stages and included cells with
367 incorrect numbers of nuclei and centrosomes as well as cells containing multiple spindles
368 (Figure 7D,E; Figure S5A,B). Thus, it appears that ectopic binding of pUbq-Cnn-C^T to γ -
369 TuRCs within spermatocytes leads to excessive cytosolic microtubules and major defects
370 during meiosis.

371

372 **Human CDK5RAP2 binding to γ -TuRCs is also regulated by auto-inhibition, but the
373 precise mechanism differs from *Drosophila***

374 To examine whether auto-inhibition is a conserved feature of CM1 domain proteins, we tested
375 the ability of various N-terminal fragments of human CDK5RAP2 (Figure 8A) to co-IP γ -tubulin
376 from HEK cell extracts. The reported CM1 domain spans aa58-126 of CDK5RAP2 (Sawin et
377 al., 2004; Zhang and Megraw, 2007) (Figure 8A) and a fragment spanning aa1-210 was less
378 efficient at co-IP'ing γ -tubulin than a fragment spanning aa51-100 (also known as γ -TuNA
379 (Choi et al., 2010)) (Figure 8B,C). This indicated that sequences either upstream or
380 downstream of γ -TuNA are inhibitory for binding to γ -TuRCs. A fragment that included the
381 sequence upstream of γ -TuNA (aa1-100) co-IP'd γ -tubulin more efficiently than γ -TuNA
382 (Figure 8B), suggesting that, unlike in *Drosophila* Cnn, the sequence upstream of the CM1
383 domain is not inhibitory but is instead required for efficient binding. In contrast, a fragment that
384 included the sequence downstream of γ -TuNA (aa51-210) was less efficient than γ -TuNA at
385 co-IP'ing γ -tubulin (Figure 8B). This suggests that the sequence downstream of the CM1
386 domain in CDK5RAP2 inhibits binding to γ -TuRCs. Thus, while auto-inhibition appears to

387 regulate the binding of CDK5RAP2 to γ -TuRCs as in flies, the precise mechanism appears to
388 vary between species.

389

390 **Discussion**

391 We have shown that the extreme N-terminal region of Cnn-C, which we name the CAI domain,
392 inhibits Cnn-C from binding to γ -TuRCs. This auto-inhibition is important because expressing
393 a form of Cnn that readily binds γ -TuRCs within the cytosol leads to spindle and cell division
394 defects, possibly via the ectopic activation of γ -TuRCs. Phospho-mimicking experiments
395 suggest that phosphorylation at sites close to the CM1 domain relieves auto-inhibition of Cnn-
396 C and promotes binding to γ -TuRCs. This is consistent with Cnn-C being phosphorylated
397 specifically at centrosomes during mitosis (Conduit et al., 2014a) where binding and activation
398 of γ -TuRCs takes place. In addition, human CDK5RAP2 is inhibited from binding cytosolic γ -
399 TuRCs by the region downstream of the CM1 domain. Thus, while the precise mechanism
400 may vary, it appears that auto-inhibition is a conserved feature of CM1 domain proteins.

401

402 There is considerable evidence, including the work presented here, showing that binding of
403 CM1-domain proteins to γ -tubulin complexes stimulates microtubule nucleation (Choi et al.,
404 2010; Muroyama et al., 2016; Hanafusa et al., 2015; Cota et al., 2017; Lynch et al., 2014), but
405 the reason remains unclear. One possibility is that binding leads to conformational changes in
406 γ -TuRCs, but human and *Xenopus* γ -TuRCs bound by CM1 domain fragments remain in an
407 open, seemingly inactive, conformation (Wieczorek et al., 2019; Liu et al., 2019). Whether this
408 is due to a low stoichiometry of binding remains unclear, but binding of the CM1 domain to *S.*
409 *cerevisiae* γ -TuSCs/ γ -TuRCs does result in structural changes that possibly promote
410 nucleation activity (Brilot et al., 2021). It is also possible that CM1 domain binding has a
411 context-specific effect. Adding CM1-domain fragments to purified γ -TuRCs within *Xenopus*
412 egg extracts had a greater effect on nucleation efficiency when the extract was supplemented
413 with activated Ran (Liu et al., 2019), and we find that expression of pUbq-Cnn-C^T leads to
414 defects within specific cell types (although these differences could simply be due to the
415 differences in expression levels). Clearly, we need a better understanding of how CM1 domain
416 binding promotes microtubule nucleation.

417

418 Phosphorylation seems to be an important mechanism for promoting binding between CM1
419 domain proteins and γ -TuRCs. This is true for human CDK5RAP2, *C. elegans* SPD-5, and *S.*
420 *cerevisiae* SPC110, where the phosphorylation sites that promote binding have been identified
421 either upstream or downstream of the CM1 domain (Hanafusa et al., 2015; Lin et al., 2014b;
422 Ohta et al., 2021). We show that phospho-mimicking sites both upstream and downstream of
423 the CM1 domain also promotes binding of *Drosophila* Cnn-C to γ -TuRCs. We predict that
424 phosphorylation helps to relieve the auto-inhibition imposed by the CAI domain as well as

425 directly increasing binding affinity between Cnn-C and γ -TuRCs. We find that phospho-
426 mimicking S¹⁸⁶ alone allows robust binding to γ -TuRCs, suggesting that phosphorylating this
427 single site is sufficient for full relief of auto-inhibition, at least *in vitro*. Phospho-mimicking T²⁷
428 has a more subtle effect but has a strong effect when S¹⁸⁶ is also phospho-mimicked. This
429 suggests that phospho-mimicking T²⁷ increases the binding affinity between Cnn-C and γ -
430 TuRCs, rather than relieving auto-inhibition, and thus has a minimal effect when Cnn-C is
431 auto-inhibited (when S¹⁸⁶ is not phospho-mimicked) but has a strong effect when Cnn-C
432 inhibition is relieved (by S¹⁸⁶ phospho-mimicking). This would suggest that the CAI domain,
433 which contains T²⁷, is also involved in binding to γ -TuRCs once inhibition is relieved. A role
434 for the region upstream of the CM1 domain in binding to γ -TuRCs may be conserved, as our
435 data shows this region is promotes binding of human CDK5RAP2 to γ -TuRCs.

436

437 In future, it will be important to understand how the CAI domain inhibits the CM1 domain. We
438 previously postulated that it might fold back and sterically inhibit the CM1 domain (Tovey et
439 al., 2018). Our data is consistent with this possibility and, in our view, this is the most likely
440 explanation. A similar mechanism has also been proposed in *C. elegans* (Ohta et al., 2021).
441 Nevertheless, there are alternative possibilities, including that the CAI domain could recruit
442 another protein that interferes with CM1 domain binding. In any case, it will be interesting to
443 compare how auto-inhibition is achieved in different homologues, especially given that the
444 region downstream, not upstream, of the CM1 domain appears to mediate inhibition in human
445 CDK5RAP2.

446

447 Importantly, our data also highlights differences in how binding between CM1 domain proteins
448 and γ -TuRCs is regulated within different cell types and at different MTOCs. Testes-specific
449 Cnn-T isoforms lack the CAI domain and recruit γ -TuRCs to mitochondria in developing sperm
450 cells (Chen et al., 2017). While we cannot rule out that Cnn-T contains autoinhibitory domains
451 in its C-terminal region, we have shown that the N-terminal region of Cnn-T can bind efficiently
452 to γ -TuRCs in the apparent absence of any upstream regulatory events. The surface of
453 mitochondria presumably lacks the kinases that regulate Cnn-C at centrosomes and so it
454 would seem appropriate that Cnn-T can bind γ -TuRCs in the absence of phosphorylation. This
455 would make most sense should Cnn-T isoforms be predominantly expressed post-meiotically,
456 which is common for testes-specific genes (White-Cooper, 2012), as their binding and
457 activation of cytosolic γ -TuRCs may perturb dividing cells but presumably would not perturb
458 developing sperm cells, which have a shrinking cytosol and no need to form a spindle.

459

460 In summary, the data presented here provide important insights into how and why binding of
461 CM1 domain proteins to γ -TuRCs is regulated. Future studies will help elucidate the precise
462 mechanism underlying auto-inhibition of the CM1 domain and how this may vary between
463 species. It will also be important to determine whether CM1 domain binding directly activates
464 γ -TuRCs and, if not, how CM1 domain binding promotes microtubule nucleation.

465 **Materials and Methods**

466

467 **DNA cloning**

468 5-alpha competent *E. coli* cells (high efficiency, NEB) were used for bacterial transformations.
469 DNA fragments were purified using QIAquick Gel Extraction kits (Qiagen); plasmid purification
470 was performed using QIAprep Spin Miniprep kits (Qiagen). Phusion high-fidelity PCR master
471 mix with HF buffer (ThermoFisher Scientific) was used for PCRs.

472

473 **Transgenic *Drosophila* lines**

474 All endogenously-tagged lines were made using CRISPR combined with homologous
475 recombination, by combining the presence of a homology-repair vector containing the desired
476 insert with the appropriate guide RNAs and Cas9. The γ -tubulin37C-mCherry and Grip128-
477 sfGFP alleles were generated by inDroso. For γ -tubulin37C-mCherry, eggs from nos-Cas9
478 expressing females were co-injected with a plasmid encoding the expression of dual guides
479 targeting each side of the 3'UTR, TACACATATCAAGATACTG and
480 CCCAGATCGATTATCCCCAG, and a plasmid containing a SSSS-mCherry-3'UTR-LoxP-
481 3xP3-dsRED-Lox P cassette flanked by homology arms (the multi-serine insert acts as a
482 flexible linker). After screening for dsRED, the selection marker was excised by Cre
483 recombination. For Grip128-sfGFP, eggs from nos-Cas9 expressing females were co-injected
484 with a plasmid encoding the expression of a single guide containing the target sequence
485 ATGGGGCACACTGGAGTTGA and with a pBluescript plasmid containing sfGFP and linker
486 sequence (4X GlyGlySer) flanked on either side by 1.5kb of DNA homologous to the genomic
487 locus surrounding the 3' end of the appropriate coding region. The homology vector was made
488 within the lab (and sent to InDroso) by HiFi assembly (NEB) of PCR fragments generated from
489 genomic DNA prepared from nos-Cas9 flies (using MicroLYSIS, Microzone) and a vector
490 containing the sfGFP tag (DGRC, 1314). Screening for the insert was performed with the
491 following primers: AGGAAGATGCGAACACACACGT and GTACAGCTCATCCATGCCA.

492

493 The Grip75-sfGFP and Grip163-sfGFP lines were made within the lab following a similar
494 approach to that used previously (Tovey et al., 2018; Mukherjee et al., 2020). Flies expressing
495 a single guide RNA containing the target sequence CAAAAACATCGTATTGATG or
496 ACCACTATTACAAGGTATCT for Grip75-sfGFP or Grip163-sfGFP, respectively, were
497 crossed to nos-Cas9 expressing females and the resulting embryos were injected with
498 homology vectors by the Department of Genetics Fly Facility, Cambridge, UK. The homology
499 vectors comprised a pBluescript plasmid containing sfGFP and linker sequence (4X

500 GlyGlySer) flanked on either side by 1.5kb of DNA homologous to the genomic locus
501 surrounding the 3' end of the appropriate coding region. The homology vectors were made as
502 for Grip128-sfGFP. F1 and F2 males were screened by PCR using the following primers: for
503 Grip75-sfGFP: GAGAAGTTGCGCATATGACCC and AGCAGCACCATGTGATCGCGC; for
504 Grip163-sfGFP: AGTCGCAGTCCTTATTGTGG and
505 AGCAGCACCATGTGATCGCGC.

506

507 pUbq-Cnn-C and pUbq-Cnn-C^T were made from a pDONR-Cnn-C vector (gift from Jordan
508 Raff). To generate a Cnn-T-specific N-terminal region of Cnn, an appropriate DNA fragment
509 (made by GENEWIZ, based on the FlyBase sequence of Cnn-T) was synthesised and
510 amplified by PCR and used to replace the N-terminal region of Cnn in a pDONR-Cnn-C vector
511 cut with XmaI. The pDONR-Cnn-C and newly made pDONR-Cnn-T vectors were then inserted
512 into a pUbq transformation vector (gift from Jordan Raff) by Gateway cloning (ThermoFisher
513 Scientific). All DNA vectors were injected into embryos by the Department of Genetics Fly
514 Facility, Cambridge, UK.

515

516 The Jupiter-mCherry line used to monitor microtubule nucleation was a gift from Jordan Raff's
517 lab. The original line was a GFP trap line from Daniel St. Johnston's lab and the GFP was
518 replaced with mCherry.

519

520 Recombinant protein cloning, expression and purification

521 Fragments of Cnn-C-N and Cnn-T-N used in co-IP experiments were amplified from the
522 pDONR-Cnn-C and pDONR-Cnn-T vectors described above by PCR and inserted into a
523 pDEST-HisMBP (Addgene, #11085) vector by Gateway cloning (Thermo Fisher Scientific).
524 Proteins were expressed in *E. coli* (BL21-DE3) and purified using affinity chromatography.
525 MBP-tagged fragments were purified by gravity flow through amylose resin (New England
526 Biolabs) and step elution in maltose. The concentration of each fraction was determined on a
527 Nanodrop and peak fractions were diluted 1:1 with glycerol and stored at -20°C. Truncated
528 fragments of Cnn-C were made by modification of the pDONR-Cnn-C-N entry clone. The N-
529 terminal region was removed by a Quikchange reaction (Agilent), and the resulting shortened
530 fragment was inserted into the pDEST-HisMBP destination vector via a Gateway reaction.

531

532 Phospho-mimetic fragments were created by modifying the pDONR-Cnn-C-N entry clone. The
533 pDONR-Cnn-C-N backbone was linearised by PCR or by digestion, omitting the phospho-
534 patch to be replaced. Phosphomimetic patches in which all S/T residues were swapped for

535 D/E residues, respectively, were synthesised either by PCR using two overlapping primers or
536 by GENEWIZ. They were inserted into the linear backbone by HiFi Assembly (NEB). The entry
537 clones were checked by restriction enzyme digest and sequencing before being inserted into
538 the pDEST-HisMBP destination vector via a Gateway reaction.

539

540 pRNA vectors were made by modification of the pDONR-Cnn-C-PReM^P vector containing
541 phospho-mimetic mutations in the PReM domain (Conduit et al., 2014a). N-terminal variants
542 were introduced by restriction digests (SspI-HF and AatII) of pDONR-Cnn-C, pDONR-Cnn-T,
543 and pDONR-Cnn-C-PReM^P entry clones. Fragments were combined as necessary by NEB
544 HiFi assembly to create new pDONR vectors, which were inserted into a pRNA-GFP or pRNA-
545 mKate destination vector (Conduit et al., 2014a) via a Gateway reaction. The Cnn-T-N
546 fragment was inserted directly into pRNA-GFP destination vectors via Gateway cloning.

547

548 Fragments of CDK5RAP2 were synthesised by Genewiz, amplified by PCR, and cloned into
549 a pCMV-GFP vector (gift from Jens Lüders) by restriction digest and HiFi assembly (NEB).

550

551 **Primers**

	Forward primer	Reverse primer
Cnn-C-N fragment	GGGGACAAGTTGTACAAAAAA GCAGGCTTAATGGACCAGTCTA AACAGGTTTG	GGGGACCACTTGTACAAGAAAG CTGGGTTCTATAGGCGCTCGGCC AAC
Cnn-T-N fragment	GGGGACAAGTTGTACAAAAAA GCAGGCTTAATGAATAGTAATC GAACGTCGTCTTCG	GGGGACCACTTGTACAAGAAAG CTGGGTTCTATAGGCGCTCGGCC AAC
Cnn-C-N ^{P1} insert	GCGGGACTATTGCGGCGACGG CAATGGTACCTGTGCAGACGAC TTGAAGGAAATCGAGTTAATTG AGGAGGTGG	GCAGGACCCTCTGTCGATTTCG GCGCGCCATTCTCCTCCAGGAA GTCCTCCACCTCCTCAATTAACT CGATTTC
Cnn-C-N ^{P2} insert	CCTGCGCAAATAGCCGAGGC ACTGGACAAAGACATAGACGAC GAGGACCCGGGAGCCCTGCAA GATGTCG	CGCCTGGAGGTGCGTGGAACGTC AAAGTCGGCATAGTCGTTCTCCA TCTCGACATCTGCAAGGGCTCCC GGGTCC
Cnn-C-N ^{P3} insert	GGGTCA GCCGGGTGCCCGGGC AGACGACGACGAGGAAGACTTA	CCTTGAGCAGCTCCATCTTACA TCGACCTCTTTCTCAACTCCGC

	GACAAACAGCTCATCGATGCCA AGATCGAAATCGC	GATTCGATCTTGGCATCGATGA GC
Cnn-C-N ^{P1a} insert	GCGGGACTATTGCGGCGACGG CAATGGTACCTGTGCAGACGAC TTGAAGGAAATCGAGTTAATTG AGACCGTGA	GGACCCTCTGTCGATTCGGCG GCGCCATTCTCCTCCAGGAAACT GGTCACGGTCTCAATTAACTCGA TTTCCTTC
Cnn-C-N ^{P1b} insert	GCGGGACTATTGCGGCGACGG CAATGGTACCTGTGCATCGTCC TTGAAGGAAATCACCTTAATTG	GGACCCTCTGTCGATTCGGCG GCGCCATTCTCCTCCAGGAAGTC CTCCACCTCCTCAATTAAGGTGA TTTCCTTC
Cnn-C-N ^{T27} insert	GCGGGACTATTGCGGCGACGG CAATGGTACCTGTGCATCGTCC TTGAAGGAAATCGAGTTAATTG AGACCGTGA	GGACCCTCTGTCGATTCGGCG GCGCCATTCTCCTCCAGGAAACT GGTCACGGTCTCAATTAACTCGA TTTCCTTC
Cnn-C-N ^{A1-77}	GCCAACTTGTACAAAAAAGCA GGCTTAATGGCCAGTTTGACG TTCC	GGAACGTCAAAACTGGCCATTAA GCCTGCTTTTGACAAAGTTG GC
CDK5RAP2 aa1-210	GGGGACAAGTTGTACAAAAAAGC AGGCTTAATGATGGACTTGGTGT GGAAGAGG	GGGGACCACTTGTACAAGAAAGCT GGGTTTCACAAGTCCCCCTCGTGCA TCTTC
CDK5RAP2 aa51-100	GGGGACAAGTTGTACAAAAAAGC AGGCTTAATGACAGTGTCTCCAC CAGAGCACG	GGGGACCACTTGTACAAGAAAGCT GGGTTTCACAAGTCCCCCTCGTGCA G
CDK5RAP2 aa51-210	GGGGACAAGTTGTACAAAAAAGC AGGCTTAATGACAGTGTCTCCAC CAGAGCACG	GGGGACCACTTGTACAAGAAAGCT GGGTTTCACAAGTCCCCCTCGTGCA TCTTC
CDK5RAP2 aa1-100	GGGGACAAGTTGTACAAAAAAGC AGGCTTAATGATGGACTTGGTGT GGAAGAGG	GGGGACCACTTGTACAAGAAAGCT GGGTTTCAGTAGATATGTTAGTGG G

552

553

554 Immunoprecipitation

555 1g/ml of embryos were homogenised with a hand-pestle in homogenisation buffer containing
 556 50 mM HEPES, pH7.6, 1mM MgCl₂, 1 mM EGTA, 50 mM KCl supplemented with PMSF 1:100,

557 Protease Inhibitor Cocktail (1:100, Sigma Aldrich) and DTT (1M, 1:1000). Extracts were
558 clarified by centrifugation twice for 15 minutes at 16,000 rcf at 4°C.

559

560 For the MBP-Cnn fragment IPs, 30 µl magnetic ProteinA dynabeads (Life Technologies)
561 coupled to anti-MBP antibodies (gift from Jordan Raff) were incubated with an excess of
562 purified MBP-Cnn fragments and rotated for 1 hour at 4°C. Unbound fragments were washed
563 off in PBST, and the saturated beads were resuspended in 100 µl embryo extract and rotated
564 at 4°C overnight. Beads were washed 5 times for 1 min each in PBST, boiled in 50 µl 2x
565 sample buffer, and separated from the sample using a magnet. Samples were analysed by
566 western blotting as described.

567

568 For the Grip-GFP IPs, 20 µl high-capacity ProteinA beads (Abcam) coupled to anti-MBP
569 antibodies (gift from Jordan Raff) were incubated with an excess of purified MBP-Cnn
570 fragments and rotated at 4°C for 1 hour. Unbound fragments were washed off in PBST and
571 the saturated beads were resuspended in 65 µl embryo extract and rotated at 4°C overnight.
572 Beads were washed 5 times for 1 min each in PBST, boiled in 2x sample buffer, and separated
573 from the sample by centrifugation. Samples were analysed by western blotting as described.

574

575 For the IPs from pUbq-Cnn-C and pUbq-Cnn-C^T embryo extract, 50 µl magnetic ProteinA
576 dynabeads (Life Technologies) coupled to anti-Cnn (C-terminal) antibodies (gift from Jordan
577 Raff) were rotated in 100 µl embryo extract at 4°C overnight. Beads were washed 5 times for
578 1 min each in PBST, boiled in 2x sample buffer, and separated from the sample using a
579 magnet. Samples were analysed by western blotting as described. We had tried these IPs
580 using beads coated with the anti-Cnn-T^N antibody but found that they did not pull down any
581 protein (data not shown), presumably as this antibody was raised against a peptide antigen
582 and recognises only denatured pUbq-Cnn-C^T on western blots.

583

584 **Electrophoresis and western blotting**

585 Samples were run on 4-20% TGX Precast Gels (BioRad) (except Figure 5C and D, in which
586 samples were run on 7.5% TGX Precast gels (BioRad)), alongside 5µl Precision Plus
587 WesternC Standard markers (BioRad). For western blotting, semi-dry blotting was carried out
588 using TransBlot Turbo 0.2µm nitrocellulose membrane transfer packs (BioRad), and a
589 TransBlot Turbo transfer system running at 1.3A, up to 25V, for 7 minutes (BioRad mixed
590 molecular weight pre-set programme). Membranes were stained with Ponceau and washed,
591 first with distilled water then with milk solution (PSBT + 4% milk powder), and then blocked in

592 milk solution for 1 hour at room temperature. Sections of blots were incubated with primary
593 antibodies as indicated in figures (antibodies found in table). Blots were incubated with
594 horseradish peroxidase (HRP)-conjugated anti-mouse, anti-rabbit, or anti-sheep secondary
595 antibodies (1:2000 in PSBT + 4% milk powder, ImmunoReagents) as appropriate for 45 mins
596 at room temperature, washed in PSBT 3 times for 15 mins each, and then incubated with ECL
597 substrate (BioRad ECL Clarity or ThermoFisher SuperSignal West Femto Max) for 5 minutes.
598 Membranes were imaged using a Kodak Image Station 4000R or a BioRad ChemiDoc.

599

600 **Mass spectrometry**

601 Samples were run into TGX Precast Gels (BioRad) and the gels were rinsed in dH₂O. Bands
602 were excised using a clean razor blade and cut into 1mm² pieces on a fresh glass slide and
603 placed into a microtube. Co-IP samples were processed by the Mass Spectrometry facility at
604 the Department of Biochemistry, University of Cambridge with LC-MS/MS analysis using a
605 Dionex Ultimate 3000 RSLC nanoUPLC (Thermo Fisher Scientific Inc, Waltham, MA, USA)
606 system and a Q Exactive Orbitrap mass spectrometer (Thermo Fisher Scientific Inc, Waltham,
607 MA, USA).

608

609 Post-run, all MS/MS data were converted to mgf files and the files were then submitted to the
610 Mascot search algorithm (Matrix Science, London UK, version 2.6.0) and searched against
611 the Uniprot Drosophila_melanogaster_20180813 database (23297 sequences; 16110808
612 residues) and common contaminant sequences containing non-specific proteins such as
613 keratins and trypsin (123 sequences; 40594 residues). Variable modifications of oxidation (M),
614 deamidation (NQ) and phosphorylation (S,T and Y) were applied as well a fixed modification
615 of carbamidomethyl (C). The peptide and fragment mass tolerances were set to 20ppm and
616 0.1 Da, respectively. A significance threshold value of p<0.05 and a peptide cut-off score of
617 20 were also applied.

618

619 **Antibodies**

620 Primary antibodies used in the study are indicated in the table below. For western blotting,
621 primary and secondary antibodies were diluted in PBST + 4% milk; primary antibodies were
622 diluted at concentrations indicated in the table; secondary antibodies were diluted at 1:2000.
623 For immunostaining, primary and secondary antibodies were diluted in PBS + 0.1% Triton
624 (PBT) + 5% BSA; primary antibodies were diluted at concentrations indicated in the table;
625 secondary antibodies (AlexaFluor 488, 561, or 633 conjugated secondary antibodies

626 (ThermoFisher)) were diluted at 1:1000 for testes and 1:1500 for embryos. DNA was stained
627 with Hoechst (Life Technologies, 33342) or DAPI.

628

Antibody	WB Concentration	IF Concentration	Source
α -Tubulin mouse monoclonal	-	1:1000	Sigma Aldrich, DM1a
Asl (N-terminal) guinea pig polyclonal	1:1000	1:1000	Gift from Jordan Raff
Cnn (N-terminal) rabbit monoclonal	1:1000	1:1000	Gift from Jordan Raff
Cnn (C-terminal) sheep polyclonal	1:1000	-	Gift from Jordan Raff
Cnn-T ^N Rabbit polyclonal	1:500	-	This study
γ -Tubulin mouse monoclonal	1:500	1:500	Sigma Aldrich, GTU-88
γ -Tubulin rabbit polyclonal	-	1:500	Sigma Aldrich, T5192
GFP mouse monoclonal	1:250 or 1:500	1:250 or 1:500	Roche, 11814460001
Grip71 rabbit polyclonal	1:100	1:100	CRB (crb2005268)
MBP rabbit polyclonal	1:3000	-	Gift from Jordan Raff
Phospho-histone H3 rabbit polyclonal	-	1:500	Abcam, AB5176
Staufen Mouse monoclonal	-	1:100	Santa Cruz dN-16
Gurken Mouse monoclonal	-	1:200	DSHB 1D12
Lamin Dm0	-	1:30	DSHB 84.12

629

630 Immunostaining

631 Testes were dissected in PBS, fixed in 4% paraformaldehyde for 30 minutes, washed 3x 5
632 minutes in PBS and incubated in 45% and then 60% acetic acid before being squashed onto
633 slides and flash-frozen in liquid nitrogen. Coverslips were removed and samples were post-
634 fixed in methanol at -20°C, washed 3x 15 minutes in PBS + 0.1% Triton (PBST), then
635 incubated overnight in a humid chamber at 4°C with primary antibodies diluted in PBST + 5%
636 BSA + 0.02% azide. Slides were washed 3x 5 minutes in PBST and then incubated for 2 hours
637 at room temperature with Alexa-Fluor secondary antibodies (ThermoFisher) (all 1:1000 in

638 PBST + 5% BSA + 0.02% azide). Slides were washed 3x 15 minutes in PBST, 10 minutes in
639 PBST with Hoechst, and then 5 minutes in PBST. 10 µl of mounting medium (85% glycerol in
640 water + 2.5% N-propyl-galate) was placed on top of the tissue and a coverslip was gently
641 lowered and sealed with nail varnish.

642

643 Embryos were collected within 2-3 hours of laying and were dechorionated in 60% bleach for
644 2 minutes. Vitelline membranes were punctured with a combination heptane and methanol +
645 3% EGTA (0.5M) before three washes in neat methanol. Embryos were fixed in methanol at
646 4°C for at least 24 hours before rehydrating. Embryos were rehydrated by washing 3x 20 mins
647 in PBST, then blocked in PBST + 5% BSA for 1 hour, followed by overnight incubation in
648 primary antibodies in PBST + 5% BSA at 4°C. Embryos were washed 3x 20 mins in PBST at
649 room temperature, then incubated for 2 hours at room temperature with Alexa-Fluor secondary
650 antibodies (ThermoFisher) (all 1:1500 in PBST + 5% BSA). Finally, embryos were washed 3x
651 20 mins in PBST at room temperature before being mounted in Vectashield containing DAPI
652 (VectorLabs).

653

654 Oocytes were dissected from 2-day-old females. For Staufen and Gurken detection, 10 to 15
655 ovaries were fixed with PBS buffer containing 4% paraformaldehyde and 0.1% Triton X-100,
656 washed three times for 5 mins in PBST and blocked in PBST containing 1% BSA. Incubation
657 with the primary antibodies (anti-Staufen, Santa Cruz; anti-Gurken 1D12, DSHB) was
658 performed overnight at room temperature or 4°C for Staufen and Gurken labelling,
659 respectively, in PBT (PBS containing 0.1% BSA and 0.1% Tween 20). The ovaries were then
660 briefly washed three times and three times for 30 min each in PBT and incubated for 2 hours
661 at room temperature in Alexa-conjugated secondary antibodies. The ovaries were then
662 washed 3x for 15 min each time in PBST, dissected, and mounted in Citifluor (Electron
663 Microscopy Science).

664

665 **Preparation of testes for phase contrast imaging of round spermatids**

666 For analysis of round spermatids under phase contrast, testes were dissected in PBS,
667 transferred to a 50µl droplet of PBS on a slide, cut open midway along the testes and, under
668 observation, gently squashed under a coverslip using blotting paper.

669

670 **mRNA preparation and injection**

671 pRNA vectors containing the appropriate cDNA were generated using Gateway cloning of
672 PCR amplified cDNA and either a pRNA-GFP or a pRNA-mKATE backbone. pRNA vectors

673 were linearised with Ascl, precipitated using EDTA, sodium acetate, and ethanol, then
674 resuspended in RNase-free water. mRNA was generated from these pRNA vectors *in vitro*
675 using a T3 mMESSAGE mMACHINE kit (ThermoFisher) and was then purified using an
676 RNeasy MinElute Cleanup kit (Qiagen). Freshly-laid unfertilised eggs were collected from
677 apple juice plates within ~1 hour of laying and were dechorionated on double-sided sticky
678 tape. Eggs were lined up on heptane glue to keep them in place during injections and imaging.
679 Embryos were dried at 25°C for ~5 mins and covered with immersion oil (Voltalef). mRNA was
680 manually injected using a syringe into eggs using needles made from borosilicate glass
681 capillary tubes, at concentrations ranging from ~2-4 µg/µl. Eggs were left for 1.5-2 hours
682 before imaging to allow for translation of the mRNA. Control eggs were injected with RNAase-
683 free water.

684

685 **Fertility tests**

686 We tested fertility rates of males and females bred at 25°C, comparing pUbq-Cnn-C^T males or
687 females to pUbq-Cnn-C males or females. We quantified the hatching rate of embryos that
688 were generated when pUbq-Cnn-C or pUbq-Cnn-C^T males or females were crossed to *w¹¹¹⁸*
689 “wild-type” flies. Cages that were sealed with apple juice agar plates with a spot of dried yeast
690 paste were set up at 25°C containing ~50 newly-hatched test flies (e.g. pUbq-Cnn-C/ -C^T) and
691 ~50 newly-hatched wild-type males or virgin females. The apple juice agar plates were
692 exchanged with fresh plates 2-4 times a day, and the removed plates were kept at 25°C for at
693 least 25 hours before the proportion of hatched eggs was calculated.

694

695 **Tissue Culture, Transfection, and IPs from HEK cells**

696 HEK293T cells were grown in high glucose GlutaMAX Dulbecco’s modified Eagle medium
697 (DMEM) supplemented with 10% heat inactivated foetal bovine serum and were incubated at
698 37°C and 5% CO₂. Cells were mycoplasma free (LookOut Mycoplasma PCR detection kit,
699 Sigma). Cells were passaged with 0.05% trypsin-EDTA every 2-3 days. 7x10⁶ cells were
700 seeded and grown for 24 hours before transfection. Cells were transfected with 1.45 µg DNA
701 using lipofectamine 2000 transfection reagent (ThermoFisher) for 4 hours in OptiMEM
702 reduced serum medium. A control flask was treated with lipofectamine 2000 in the absence
703 of any DNA but was otherwise processed identically. The medium was replaced with DMEM,
704 and cells were allowed to grow for a further 16 hours before harvesting for
705 immunoprecipitation.

706

707 Transfected cells were washed twice in PBS and lysed in buffer (50 mM HEPES, pH7.5, 150
708 mM NaCl, 1mM MgCL₂, 1mM EGTA, 0.5% IGEPAL and protease inhibitors), and rotated for
709 90 minutes at 4°C. Cells were harvested at 15,000 rpm, 10 mins, 4°C. The supernatant was
710 mixed with 30 µl GFP-Trap_MA beads (Chromotek) and rotated overnight at 4°C. Beads were
711 washed 3 times in ice cold PBST, then resuspended in 50 µl 2x Laemmli sample buffer and
712 boiled for 10 minutes at 95°C. Western blots were run as described above, using anti-GFP
713 (1:250) (mouse, Roche) and anti-gamma-Tubulin (1:250) (rabbit, T5192 Sigma) primary
714 antibodies.

715

716 **Microscopy**

717 All imaging was carried out at room temperature (~20°C). Confocal imaging of fixed embryo
718 (and the movies of scaffolds organising microtubules) was carried out on an Olympus FV3000
719 scanning inverted confocal system run by FV-OSR software using a 60X 1.4NA silicone
720 immersion lens (UPLSAPO60xSilicone) or x30 0.95NA silicone immersion lens
721 (UPLSAPO30xSilicone). Confocal imaging of scaffolds recruiting γ-TuRC proteins or
722 organising microtubules and of testes samples was carried out on a Zeiss Axio Observer.Z1
723 inverted CSU-X1 Yokogawa spinning disk system with 2 ORCA Fusion camera (Hamamatsu)
724 run by Zeiss Zen2 acquisition software using a 60X 1.4NA oil immersion lens (Zeiss). Confocal
725 imaging of oocytes was carried out on a Confocal LSM780 mount on a Axio Observer Z1
726 microscope (Zeiss), detection with spectral channels GaAsP, controlled by Zen software using
727 a 25X 0.8NA Plan Apochromat Oil objective. Phase contrast microscopy of round spermatids
728 was performed on a Leica DM IL LED inverted microscope controlled by µManager software
729 and coupled to a RetigaR1 monochrome camera (QImaging) using a 40X 0.55NA air objective
730 (Leica).

731

732 **Image and statistical analysis**

733 All images were processed using Fiji (ImageJ). *Quantifying and comparing the intensity of Cnn*
734 *and γ-TuRC components at Cnn scaffolds:* Maximum intensity Z-plane projections were made
735 and a threshold mask was generated using the Cnn channel. Sum fluorescence intensities for
736 the Cnn and γ-TuRC protein channels were calculated. Overall mean cytosolic background
737 intensity measurements for each channel were used to “background correct” the sum
738 intensities for each scaffold. The scaffold intensities within each egg were plotted in Prism and
739 a weighted linear regression analysis (based on ensuring an even distribution of residuals
740 across the X axis) was performed. The gradient of the weighted regression line represented
741 the S value for a given egg. The distribution of the S values per condition were lognormally

742 distributed (as determined by Anderson-Darling, D'Agostino and Pearson, Shapiro-Wilk, and
743 Kolmogorov-Smirnov tests) and so, to compare mean S values, the \log_{10} of each individual S
744 value was first calculated before performing a one-way ANOVA analysis (Dunnett's multiple
745 comparisons test). This was to ensure the data being compared was normally distributed.
746 Nevertheless, the unadjusted S values were plotted. Note that the fluorescence values and S
747 values are in arbitrary units and cannot be directly compared between the γ -tubulin-mCherry
748 and Grip75-sfGFP analysis. *Blind analysis of Cnn scaffolds organising microtubules:* Images
749 were blinded ensuring each image had the same contrast settings. Images were then selected
750 on scaffold size, with eggs containing small or very large scaffolds removed. The remaining
751 images were then scored by eye as being of eggs that contained scaffolds with either no
752 asters, weak or strong asters, or scaffolds where the Jupiter-mCherry signal did not extend
753 beyond the GFP-Cnn signal (overlay). *Blind analysis of pUbq-Cnn-C or pUbq-Cnn-C^T*
754 *embryos:* Images were blinded ensuring each image had the same contrast settings. Embryos
755 were then scored by eye as being either normal or having moderate or severe defects.
756 Embryos were scored as normal even when one or two mitotic figures had defects, because
757 this is quite common in syncytial embryos and does not prevent development. Embryos were
758 scored as having moderate defects when an unusually high proportion of mitotic figures had
759 defects, or where the overall organisation of the spindles was moderately abnormal. Embryos
760 were scored as having severe defects when there was either massive disorder with individual
761 mitotic figures or overall organisation, or both. *To quantify western blot bands:* the sum
762 intensities of bands were background corrected using mean "background" values at positions
763 on the gel with no apparent signal. To reduce variation, the band intensities were taken using
764 the freehand tool to draw closely around the perimeter of the band. For the Co-IP experiments,
765 the intensities of the γ -tubulin IP bands were normalised to the intensity of the γ -tubulin band
766 in the MBP-Cnn-T-N IP within each experiment. GraphPad Prism 7 or 8 was used for all
767 statistical analysis and graph production.

768

769 **Bioinformatics**

770 Protein alignments were produced using JalView. Secondary structure predictions were
771 performed using JPred 4.

772

773 **Online Supplemental material**

774 Fig. S1 shows the different constructs that were used in the study. Fig. S2 shows that MBP-
775 Cnn-T-N fragments co-immunoprecipitate various γ -TuRC proteins. Fig. S3 shows alignments
776 of the N-terminal region of Cnn-C from different *Drosophila* species and with homologues from

777 more diverse species. Fig. S4 shows images of Staufen and Gurken localisation within pUbq-
778 Cnn-C or pUbq-Cnn-T oocytes. Fig. S5 shows images of spermatocytes stained for DNA,
779 centrosomes and microtubules within pUbq-Cnn-C or pUbq-Cnn-T testes. Videos 1-4 show
780 Cnn-T scaffolds organising microtubules, including asters and spindle-like structures. Video 5
781 shows dynamic cytosolic microtubules within eggs injected with mRNA encoding GFP-Cnn-T-
782 N.

783

784 **Acknowledgements**

785 This research was supported by a Wellcome Trust and Royal Society Sir Henry Dale
786 fellowship [105653/Z/14/Z] and by an IdEx Université de Paris ANR-18-IDEX-0001 awarded
787 to PTC, by a Glover Fund research fellowship (Clare College/Dept. of Biochemistry, University
788 of Cambridge) awarded to CAT, by an Association pour la Recherche sur le Cancer grant
789 (PJA 20181208148) awarded to AG, and by the CNRS. We thank Jordan Raff for sharing
790 reagents, Berthold Hedwig and Steve Rogers for help with needle pulling, Jens Lüders for
791 sharing the pCMV-GFP vector, and Matt Castle for guidance on statistical analysis. We thank
792 other members of the Conduit lab for their invaluable input. The work benefited from the
793 Imaging Facility, Department of Zoology, University of Cambridge, supported by Matt Wayland
794 and a Sir Isaac Newton Trust Research Grant (18.07ii(c)), from the ImagoSeine at the IJM,
795 Paris, and from use of the Cambridge Centre for Proteomics Core Facility. For the purpose of
796 Open Access, the author has applied a CC BY public copyright license to any Author Accepted
797 Manuscript version arising from this submission. The authors declare no competing financial
798 interests.

799

800

801 **Author Contributions**

802 Paul Conduit: Funding acquisition, conceptualization, project administration, formal analysis,
803 investigation, resources, supervision, validation, visualization, writing original draft and review
804 & editing. Corinne Tovey: Funding acquisition, conceptualization, formal analysis,
805 investigation, supervision, validation, writing - review & editing. Chisato Tsuji: formal analysis,
806 investigation. Alice Egerton: investigation. Marc de la Roche: investigation, resources. Antoine
807 Guichet: resources, investigation, formal analysis, validation. Fred Bernard: resources

808

809

810

811 **References**

812
813

- 814 Brilot, A., A. Lyon, A. Zelter, S. Viswanath, A. Maxwell, M.J. MacCoss, E.G. Muller, A. Sali, T.N.
815 Davis, and D.A. Agard. 2021. CM1-driven assembly and activation of Yeast γ -Tubulin Small
816 Complex underlies microtubule nucleation. *BioRxiv*. doi:10.1101/2020.11.21.392803.
- 817 Chen, J.V., R.A. Buchwalter, L.-R. Kao, and T.L. Megraw. 2017. A Splice Variant of Centrosomin
818 Converts Mitochondria to Microtubule-Organizing Centers. *Curr Biol.* 27:1928–1940.e6.
819 doi:10.1016/j.cub.2017.05.090.
- 820 Choi, Y.-K., P. Liu, S.K. Sze, C. Dai, and R.Z. Qi. 2010. CDK5RAP2 stimulates microtubule nucleation
821 by the γ -tubulin ring complex. *J Cell Biology*. 191:1089–1095. doi:10.1083/jcb.201007030.
- 822 Conduit, P.T., Z. Feng, J.H. Richens, J. Baumbach, A. Wainman, S.D. Bakshi, J. Dobbelaere, S.
823 Johnson, S.M. Lea, and J.W. Raff. 2014a. The centrosome-specific phosphorylation of Cnn by
824 Polo/Plk1 drives Cnn scaffold assembly and centrosome maturation. *Dev Cell.* 28:659–669.
825 doi:10.1016/j.devcel.2014.02.013.
- 826 Conduit, P.T., J.H. Richens, A. Wainman, J. Holder, C.C. Vicente, M.B. Pratt, C.I. Dix, Z.A. Novak,
827 I.M. Dobbie, L. Schermelleh, and J.W. Raff. 2014b. A molecular mechanism of mitotic centrosome
828 assembly in Drosophila. *Elife*. 3:2987. doi:10.7554/elife.03399.
- 829 Consolati, T., J. Locke, J. Roostalu, Z.A. Chen, J. Gannon, J. Asthana, W.M. Lim, F. Martino, M.A.
830 Cvetkovic, J. Rappaport, A. Costa, and T. Surrey. 2020. Microtubule Nucleation Properties of
831 Single Human γ TuRCs Explained by Their Cryo-EM Structure. *Dev Cell.*
832 doi:10.1016/j.devcel.2020.04.019.
- 833 Cota, R.R., N. Teixidó-Travesa, A. Ezquerra, S. Eibes, C. Lacasa, J. Roig, and J. Lüders. 2017. MZT1
834 regulates microtubule nucleation by linking γ TuRC assembly to adapter-mediated targeting and
835 activation. *J Cell Sci.* 130:jcs.195321. doi:10.1242/jcs.195321.
- 836 Eisman, R.C., M.A.S. Phelps, and T. Kaufman. 2015. An Amino-Terminal Polo Kinase Interaction
837 Motif Acts in the Regulation of Centrosome Formation and Reveals a Novel Function for
838 centrosomin (cnn) in Drosophila. *Genetics*. 201:685–706. doi:10.1534/genetics.115.181842.

- 839 Eisman, R.C., M.A.S. Phelps, and T.C. Kaufman. 2009. Centrosomin: a complex mix of long and short
840 isoforms is required for centrosome function during early development in *Drosophila melanogaster*.
841 *Genetics*. 182:979–997. doi:10.1534/genetics.109.103887.
- 842 Farache, D., L. Emorine, L. Haren, and A. Merdes. 2018. Assembly and regulation of γ -tubulin
843 complexes. *Open Biol.* 8:170266. doi:10.1098/rsob.170266.
- 844 Feng, Z., A. Caballe, A. Wainman, S. Johnson, A.F.M. Haensele, M.A. Cottee, P.T. Conduit, S.M. Lea,
845 and J.W. Raff. 2017. Structural Basis for Mitotic Centrosome Assembly in Flies. *Cell*. 169:1078
846 1089.e13. doi:10.1016/j.cell.2017.05.030.
- 847 Flor-Parra, I., A.B. Iglesias-Romero, and F. Chang. 2018. The XMAP215 Ortholog Alp14 Promotes
848 Microtubule Nucleation in Fission Yeast. *Curr Biol*. 28:1681–1691.e4.
849 doi:10.1016/j.cub.2018.04.008.
- 850 Gunzelmann, J., D. Rüthnick, T. Lin, W. Zhang, A. Neuner, U. Jäkle, and E. Schiebel. 2018. The
851 microtubule polymerase Stu2 promotes oligomerization of the γ -TuSC for cytoplasmic microtubule
852 nucleation. *Elife*. 7:934. doi:10.7554/elife.39932.
- 853 Hanafusa, H., S. Kedashiro, M. Tezuka, M. Funatsu, S. Usami, F. Toyoshima, and K. Matsumoto. 2015.
854 PLK1-dependent activation of LRRK1 regulates spindle orientation by phosphorylating
855 CDK5RAP2. *Nat Cell Biol*. 17:1024–1035. doi:10.1038/ncb3204.
- 856 Hutchins, J.R.A., Y. Toyoda, B. Hegemann, I. Poser, J.-K. Hériché, M.M. Sykora, M. Augsburg, O.
857 Hudecz, B.A. Buschhorn, J. Bulkescher, C. Conrad, D. Comartin, A. Schleiffer, M. Sarov, A.
858 Pozniakovsky, M.M. Slabicki, S. Schloissnig, I. Steinmacher, M. Leuschner, A. Ssykor, S. Lawo,
859 L. Pelletier, H. Stark, K. Nasmyth, J. Ellenberg, R. Durbin, F. Buchholz, K. Mechtler, A.A. Hyman,
860 and J.-M. Peters. 2010. Systematic Analysis of Human Protein Complexes Identifies Chromosome
861 Segregation Proteins. *Science*. 328:593–599. doi:10.1126/science.1181348.
- 862 Kollman, J.M., C.H. Greenberg, S. Li, M. Moritz, A. Zelter, K.K. Fong, J.-J. Fernandez, A. Sali, J.
863 Kilmartin, T.N. Davis, and D.A. Agard. 2015. Ring closure activates yeast γ TuRC for species-
864 specific microtubule nucleation. *Nat Struct Mol Biol*. 22:132–137. doi:10.1038/nsmb.2953.
- 865 Kollman, J.M., A. Merdes, L. Mourey, and D.A. Agard. 2011. Microtubule nucleation by γ -tubulin
866 complexes. *Nat Rev Mol Cell Bio*. 12:709–721. doi:10.1038/nrm3209.
- 867 Lin, T., A. Neuner, and E. Schiebel. 2014a. Targeting of γ -tubulin complexes to microtubule organizing
868 centers: conservation and divergence. *Trends Cell Biol*. 25:296–307. doi:10.1016/j.tcb.2014.12.002.

- 869 Lin, T., A. Neuner, Y.T. Schlosser, E. Schiebel, A.N. Scharf, and L. Weber. 2014b. Cell-cycle
870 dependent phosphorylation of yeast pericentrin regulates γ -TuSC-mediated microtubule nucleation.
871 *Elife*. 3:e02208. doi:10.7554/elife.02208.
- 872 Liu, P., Y.-K. Choi, and R.Z. Qi. 2014. NME7 is a functional component of the γ -tubulin ring complex.
873 *Mol Biol Cell*. 25:2017–2025. doi:10.1091/mbc.e13-06-0339.
- 874 Liu, P., E. Zupa, A. Neuner, A. Böhler, J. Loerke, D. Flemming, T. Ruppert, T. Rudack, C. Peter, C.
875 Spahn, O.J. Gruss, S. Pfeffer, and E. Schiebel. 2019. Insights into the assembly and activation of the
876 microtubule nucleator γ -TuRC. *Nature*. 1–8. doi:10.1038/s41586-019-1896-6.
- 877 Lynch, E.M., L.M. Grocock, W.E. Borek, and K.E. Sawin. 2014. Activation of the γ -Tubulin Complex
878 by the Mto1/2 Complex. *Curr Biol*. 24:896 903. doi:10.1016/j.cub.2014.03.006.
- 879 Mukherjee, A., P.S. Brooks, F. Bernard, A. Guichet, and P.T. Conduit. 2020. Microtubules originate
880 asymmetrically at the somatic Golgi and are guided via Kinesin2 to maintain polarity in neurons.
881 *Elife*. 9:e58943. doi:10.7554/elife.58943.
- 882 Muroyama, A., L. Seldin, and T. Lechler. 2016. Divergent regulation of functionally distinct γ -tubulin
883 complexes during differentiation. *J Cell Biology*. 213:679–692. doi:10.1083/jcb.201601099.
- 884 Nithianantham, S., B.D. Cook, M. Beans, F. Guo, F. Chang, and J. Al-Bassam. 2018. Structural basis
885 of tubulin recruitment and assembly by microtubule polymerases with Tumor Overexpressed Gene
886 (TOG) domain arrays. *Elife*. 7:e38922. doi:10.7554/elife.38922.
- 887 Oegema, K., C. Wiese, O.C. Martin, R.A. Milligan, A. Iwamatsu, T.J. Mitchison, and Y. Zheng. 1999.
888 Characterization of two related Drosophila gamma-tubulin complexes that differ in their ability to
889 nucleate microtubules. *The Journal of cell biology*. 144:721 733.
- 890 Ohta, M., Z. Zhao, D. Wu, S. Wang, J.L. Harrison, J.S. Gómez-Cavazos, A. Desai, and K.F. Oegema.
891 2021. Polo-like kinase 1 independently controls microtubule-nucleating capacity and size of the
892 centrosome. *J Cell Biol*. 220. doi:10.1083/jcb.202009083.
- 893 Petry, S., and R.D. Vale. 2015. Microtubule nucleation at the centrosome and beyond. *Nat Cell Biol*.
894 17:1089 1093. doi:10.1038/ncb3220.
- 895 Pinyol, R., J. Scrofani, and I. Vernos. 2013. The role of NEDD1 phosphorylation by Aurora A in
896 chromosomal microtubule nucleation and spindle function. *Curr Biol*. 23:143 149.
897 doi:10.1016/j.cub.2012.11.046.

- 898 Roostalu, J., N.I. Cade, and T. Surrey. 2015. Complementary activities of TPX2 and chTOG constitute
899 an efficient importin-regulated microtubule?nucleation module. *Nat Cell Biol.* 17:1422 1434.
900 doi:10.1038/ncb3241.
- 901 Sanchez, A.D., and J.L. Feldman. 2016. Microtubule-organizing centers: from the centrosome to non-
902 centrosomal sites. *Curr Opin Cell Biol.* 44:93 101. doi:10.1016/j.ceb.2016.09.003.
- 903 Sawin, K.E., P.C.C. Lourenço, and H.A. Snaith. 2004. Microtubule nucleation at non-spindle pole body
904 microtubule-organizing centers requires fission yeast centrosomin-related protein mod20p. *Curr*
905 *Biol.* 14:763 775. doi:10.1016/j.cub.2004.03.042.
- 906 Scrofani, J., T. Sardon, S. Meunier, and I. Vernos. 2015. Microtubule nucleation in mitosis by a
907 RanGTP-dependent protein complex. *Curr Biol.* 25:131 140. doi:10.1016/j.cub.2014.11.025.
- 908 Tariq, A., L. Green, J.C.G. Jeynes, C. Soeller, and J.G. Wakefield. 2020. In vitro reconstitution of
909 branching microtubule nucleation. *Elife.* 9:e49769. doi:10.7554/elife.49769.
- 910 Teixidó-Travesa, N., J. Roig, and J. Lüders. 2012. The where, when and how of microtubule nucleation
911 - one ring to rule them all. *J Cell Sci.* 125:4445 4456. doi:10.1242/jcs.106971.
- 912 Thawani, A., R.S. Kadzik, and S. Petry. 2018. XMAP215 is a microtubule nucleation factor that
913 functions synergistically with the γ -tubulin ring complex. *Nat Cell Biol.* 20:1 18.
914 doi:10.1038/s41556-018-0091-6.
- 915 Thawani, A., M.J. Rale, N. Coudray, G. Bhabha, H.A. Stone, J.W. Shaevitz, and S. Petry. 2020. The
916 transition state and regulation of γ -TuRC-mediated microtubule nucleation revealed by single
917 molecule microscopy. *Elife.* 9:e54253. doi:10.7554/elife.54253.
- 918 Tillery, M., C. Blake-Hedges, Y. Zheng, R. Buchwalter, and T. Megraw. 2018. Centrosomal and Non-
919 Centrosomal Microtubule-Organizing Centers (MTOCs) in *Drosophila melanogaster*. *Cells.* 7:121.
920 doi:10.3390/cells7090121.
- 921 Tovey, C.A., and P.T. Conduit. 2018. Microtubule nucleation by γ -tubulin complexes and beyond.
922 *Essays Biochem.* 91:EBC20180028. doi:10.1042/ebc20180028.
- 923 Tovey, C.A., C.E. Tubman, E. Hamrud, Z. Zhu, A.E. Dyas, A.N. Butterfield, A. Fyfe, E. Johnson, and
924 P.T. Conduit. 2018. γ -TuRC Heterogeneity Revealed by Analysis of Mozart1. *Curr Biol.* 28:2314
925 2323.e6. doi:10.1016/j.cub.2018.05.044.

- 926 White-Cooper, H. 2012. Tissue, cell type and stage-specific ectopic gene expression and RNAi
927 induction in the *Drosophila* testis. *Spermatogenesis*. 2:11–22. doi:10.4161/spmg.19088.
- 928 Wieczorek, M., S. Bechstedt, S. Chaaban, and G.J. Brouhard. 2015. Microtubule-associated proteins
929 control the kinetics of microtubule nucleation. *Nat Cell Biol.* 17:907 916. doi:10.1038/ncb3188.
- 930 Wieczorek, M., L. Urnavicius, S.-C. Ti, K.R. Molloy, B.T. Chait, and T.M. Kapoor. 2019. Asymmetric
931 Molecular Architecture of the Human γ -Tubulin Ring Complex. *Cell*.
932 doi:10.1016/j.cell.2019.12.007.
- 933 Woodruff, J.B., B.F. Gomes, P.O. Widlund, J. Mahamid, A. Honigmann, and A.A. Hyman. 2017. The
934 Centrosome Is a Selective Condensate that Nucleates Microtubules by Concentrating Tubulin. *Cell*.
935 169:1066 1077.e10. doi:10.1016/j.cell.2017.05.028.
- 936 Zhang, J., and T.L. Megraw. 2007. Proper recruitment of gamma-tubulin and D-TACC/Msp's to
937 embryonic *Drosophila* centrosomes requires Centrosomin Motif 1. *Mol Biol Cell*. 18:4037 4049.
938 doi:10.1091/mbc.e07-05-0474.
- 939
- 940

941 **Figure Legends**

942

943 **Figure 1**

944 **The extreme N-terminal region of Cnn-C inhibits binding to γ -tubulin complexes. (A)**

945 Diagram of the centrosomal Cnn (Cnn-C) and testes-specific Cnn (Cnn-T) isoforms that exist
946 *in vivo*. **(B)** Diagram of artificial Cnn proteins with differing N-terminal regions used to form
947 Cnn scaffolds (induced by phospho-mimetic mutations in the PReM domain (beige)) via
948 mRNA injection into unfertilised eggs. **(C-F)** Fluorescence images of unfertilised eggs
949 expressing γ -tubulin37C-mCherry that were injected with mRNA encoding different types of
950 artificial Cnn protein, as indicated. Insets show representative examples of individual
951 scaffolds. **(G)** Graph showing fluorescence intensity measurements (in arbitrary units) of γ -
952 tubulin37C-mCherry and GFP-Cnn at Cnn-C (n= 1498 scaffolds; 12 eggs), Cnn-T (n= 1400
953 scaffolds; 10 eggs), Cnn-C $^{\Delta 1-77}$ (n= 2168 scaffolds; 10 eggs), or Cnn-C $^{\Delta 1-97}$ (n= 400 scaffolds;
954 7 eggs) scaffolds. Each dot represents a single scaffold. **(H)** Graph shows slope values of
955 linear regression lines calculated for scaffolds of different types. Each slope value represents
956 an individual egg that contained multiple scaffolds. The geometric mean and 95% CIs are
957 indicated. P values are from comparisons to the Cnn-C mean using a one-way ANOVA of
958 log₁₀ transformed data. **(I,J)** Western blot of a co-IP experiment (I) and quantification of γ -
959 tubulin bands (J) showing the efficiency with which different MBP-tagged N-terminal fragments
960 of Cnn, as indicated, co-IP γ -tubulin from embryo extracts. γ -tubulin band intensities were
961 normalised within each of 3 experimental repeats to the γ -tubulin band in the respective MBP-
962 Cnn-T-N IP.

963

964 **Figure 2**

965 **The γ -TuRC-specific protein Grip75^{GCP4} is recruited strongly to Cnn-T and Cnn-C $^{\Delta 1-77}$
966 scaffolds.** Fluorescence images **(A-C)** show mKATE-Cnn scaffolds of different types, as
967 indicated, within eggs expressing endogenously-tagged Grip75^{GCP4}-sfGFP. Insets in show
968 representative examples of individual scaffolds. **(D)** Graph showing fluorescence intensity
969 measurements (in arbitrary units) of Grip75^{GCP4}-sfGFP and mKATE-Cnn at Cnn-C (n= 1920
970 scaffolds; 12 eggs), Cnn-T (n= 1650 scaffolds; 10 eggs) or Cnn-C $^{\Delta 1-77}$ (n= 2599 scaffolds; 10
971 eggs). Each dot represents a single scaffold. **(E)** Graph shows slope values of linear
972 regression lines calculated for scaffolds of different types. Each slope value represents an
973 individual egg that contained multiple scaffolds. The mean and 95% CIs are indicated. P
974 values are from comparisons to the Cnn-C mean using a one-way ANOVA.

975

976 **Figure 3**
977 **Cnn-T and Cnn-C^{Δ1-77} scaffolds organise microtubules more robustly than Cnn-C**
978 **scaffolds. (A-C)** Fluorescence images of Cnn-C scaffolds (A), Cnn-T scaffolds (B), or Cnn-
979 C^{Δ1-77} scaffolds (C) within eggs expressing the microtubule marker Jupiter-mCherry. (D) Bar-
980 graph showing results of a blind categorisation of eggs containing the different scaffold types
981 based on the ability of the scaffolds within each egg to organise microtubule asters (numbers
982 of eggs analysed indicated above). (E,F) Fluorescence images showing that adjacent Cnn-T
983 (E) or Cnn-C^{Δ1-77} (F) scaffolds can organise spindle-like structures.

984

985 **Figure 4**
986 **Phospho-mimetic mutations within the CAI domain and downstream of the CM1 domain**
987 **promote binding to γ-tubulin complexes. (A)** A cartoon showing the N-terminal region (aa1-
988 255) of Cnn used in co-IP experiments. Regions of potential phosphorylation sites are
989 indicated, with their amino acid sequence displayed. (B-F) Western blots of co-IP experiments
990 (B,C,E) and quantification of γ-tubulin bands (D,F) showing the efficiency to which different
991 MBP-tagged N-terminal fragments of Cnn, as indicated, co-IP γ-tubulin from extracts of wild-
992 type embryo (B-F), or γ-tubulin (top panels in E) and Grip75^{GCP4}-sfGFP (bottom panels in E)
993 from extracts of Grip75^{GCP4}-sfGFP-expressing embryos. In (D) and (F), band intensities were
994 normalised within each experiment to the γ-tubulin band in the respective MBP-Cnn-T-N IP.
995 The connecting lines indicate data points obtained from within the same experiment. P values
996 are from comparisons to the Cnn-C mean using either Wilcoxon matched-pairs signed rank
997 tests (D, n=9 for comparison with Cnn-C-N^{T27}; n=5 for comparison with Cnn-C-N^{P1}) or a Dunn's
998 multiple comparisons test (F, n=4). (G,H) Graphs showing the S values from eggs expressing
999 either γ-tubulin-mCherry (G) or Grip75^{GCP4}-sfGFP (H) which contain the indicated scaffold
1000 types. Note that the data for Cnn-C, Cnn-T, and Cnn-C^{Δ1-77} scaffolds is the same as in Figures
1001 1H and 2E to allow comparisons with the phospho-mimetic scaffolds. In (G) n= 2650 scaffolds
1002 and 11 eggs for Cnn-C^{T27} scaffolds, 1803 scaffolds and 11 eggs for Cnn-C^{T186} scaffolds, 2482
1003 scaffolds and 10 eggs for Cnn-C^{T173} scaffolds, and 2835 scaffolds and 18 eggs for Cnn-
1004 C^{T27,S186} scaffolds. In (H) n= 1448 scaffolds and 10 eggs for Cnn-C^{T27} scaffolds, 1074 scaffolds
1005 and 10 eggs for Cnn-C^{T186} scaffolds, and 943 scaffolds and 10 eggs for Cnn-C^{T27,S186} scaffolds.
1006 The geometric mean and 95% CIs are indicated. ** indicates p<0.01, n.s. indicates p>0.05. P
1007 values were from comparisons to the Cnn-C mean using a one-way ANOVA of log₁₀
1008 transformed data. (I) Bar-graph showing results of a blind categorisation of eggs containing
1009 the different scaffold types based on the ability of the scaffolds within each egg to organise
1010 microtubule asters (numbers of eggs analysed indicated above). Note that the data for Cnn-

1011 C, Cnn-T, and Cnn-C^{Δ1-77} scaffolds is the same as in Figure 3D to allow comparisons with the
1012 phospho-mimetic scaffolds.

1013

1014 **Figure 5**

1015 **Expression of pUbq-Cnn-C^T, which ectopically binds γ-TuRCs, reduces the ability of**
1016 **flies to generate progeny. (A)** Diagram of normal Cnn-C and chimeric Cnn-C^T in which the
1017 CAI domain of Cnn-C (dark blue) is replaced by the shorter N-terminus of Cnn-T (red). **(B)**
1018 Graph showing the proportion of embryos that hatched from crosses of wild type flies to 0-1-
1019 or 1-2-week old pUbq-Cnn-C or pUbq-Cnn-C^T males or females, as indicated. Means and 95%
1020 confidence intervals are indicated. Total numbers of embryos counted and number of counts
1021 are indicated below. **(C)** Western blots of protein extracts from embryos and testes of wild-
1022 type (WT), pUbq-Cnn-C, and pUbq-Cnn-C^T flies, as indicated. Blots were probed with anti-γ-
1023 tubulin, anti-Cnn-C (N-term), anti-Cnn-C (C-term), and anti-Cnn-T^N antibodies as indicated.
1024 Note that endogenous Cnn-C (black arrowheads) runs at the same height as pUbq-Cnn-C
1025 (blue arrowheads) on these blots, explaining the increased brightness of these bands in the
1026 pUbq-Cnn-C extract lanes. Note also that the C-terminal Cnn-C antibody recognises an
1027 unspecific band (asterisks) of approximately the same size as pUbq-Cnn-C^T (red arrowheads)
1028 and thus the pUbq-Cnn-C^T band intensity would be lower in the absence of this unspecific
1029 band. **(D)** Western blot showing co-IP of γ-tubulin via anti-Cnn antibodies from embryo
1030 extracts expressing either pUbq-Cnn-C or pUbq-Cnn-C^T, as indicated. Red arrowhead
1031 indicates Cnn-C^T. Note that, given the low expression of pUbq-Cnn-C^T within embryos, gel
1032 loading of the IP lanes was adjusted to better balance the amount of Cnn protein per lane.

1033

1034 **Figure 6**

1035 **Expression of pUbq-Cnn-C^T increases the frequency of nuclear and spindle defects**
1036 **observed within syncytial embryos. (A-F)** Fluorescence images of syncytial embryos
1037 expressing either pUbq-Cnn-C (A-C) or pUbq-Cnn-C^T (D-F) in either S-phase/prophase (A,D)
1038 Metaphase (B,E), or telophase (C,F). Note the apparent high density of cytosolic microtubules
1039 that can be (but are not always) observed in pUbq-Cnn-C^T embryos, along with major
1040 organisation defects. **(G)** Graph showing results from a blind categorisation of wild-type
1041 (n=49), pUbq-Cnn-C (n=88), or pUbq-Cnn-C^T (n=36) embryos based on the presence or
1042 absence of moderate or severe nuclear or spindle defects. **(H)** Fluorescence images of an
1043 egg expressing the microtubule marker Jupiter-mCherry (magenta) that had been injected
1044 with mRNA encoding GFP-Cnn-T-N (green).

1045

1046 **Figure 7**
1047 **Expression of pUbq-Cnn-C^T results in major defects during male meiosis.** **(A,B)** Phase
1048 contrast images showing round spermatids from testes of flies expressing pUbq-Cnn-C (A) or
1049 pUbq-Cnn-C^T (B). Alterations in nucleus: nebenkern ratio (normally 1:1, asterisks in right
1050 panel) and size (normally approximately equal) indicate defects in cytokinesis and
1051 karyokinesis. **(C)** Graph showing quantification of the nucleus:nebenkern ratio (left panel -
1052 means and standard deviations indicated) and variance in nuclear diameter (right panel –
1053 geometric means and 95% CIs indicated, p value from an unpaired t-test of log₁₀-transformed
1054 data) in pUbq-Cnn-C (n=22 cysts) and pUbq-Cnn-C^T (n=27 cysts) testes. **(D,E)** Fluorescence
1055 images showing spermatocytes or round spermatids at different developmental stages, as
1056 indicated, from testes of flies expressing pUbq-Cnn-C (D) or pUbq-Cnn-C^T (E) stained for
1057 microtubules (green, α -tubulin), centrosomes (pink, Asterless), and DNA (blue). Defects within
1058 cells expressing pUbq-Cnn-C^T include an apparent high density of cytosolic microtubules,
1059 abnormal spindles, and too many nuclei.

1060
1061 **Figure 8**
1062 **The region downstream of the CM1 domain in human CDK5RAP2 is inhibitory for**
1063 **binding to γ -TuRCs.** **(A)** Cartoon depicting the various CDK5RAP2 N-terminal fragments
1064 used in IP experiments and indicating their relative γ -TuRC binding affinity. **(B,C)** Western
1065 blots of co-IP experiments from HEK cell extracts probed for the various GFP-tagged
1066 CDK5RAP2 fragments (top) and γ -tubulin (bottom).

1067

1068 **Supplementary Figure Legends**

1069

1070 **Figure S1**

1071 **Diagrams of different Cnn constructs (omitting the tags) used in this study.** **(A)** Diagram
1072 showing full-length Cnn constructs without modifications to the PReM domain. Cnn-T is the
1073 testes-specific isoform in *Drosophila*. Cnn-C is the major centrosomal isoform in *Drosophila*.
1074 Cnn-C^T represents an artificial form of Cnn-C in which the N-terminal region of Cnn-C (dark
1075 blue) has been replaced with the N-terminal region of Cnn-T (red). **(B)** Diagram showing Cnn
1076 constructs used in the scaffold assay, where Cnn-C contains phospho-mimetic mutations in
1077 the PReM domain to drive scaffold formation *in vivo*. **(C)** Diagram showing bacterially-purified
1078 N-terminal fragments of different Cnn types used in co-IP experiments.

1079

1080 **Figure S2**

1081 **Bacterially-purified MBP-Cnn-T-N fragments immunoprecipitate γ-Tubulin Ring
1082 Complexes.** **(A)** Western blot showing results of anti-MBP immunoprecipitation from embryo
1083 extracts expressing GFP-tagged Grip proteins (homologues of GCP4,5,6), either
1084 supplemented (+) or not supplemented (-) with MBP-Cnn-T-N, as indicated. Blots were probed
1085 with anti-GFP, anti-Grip71 and anti-γ-tubulin antibodies as indicated. When using MBP-Cnn-
1086 T-N, γ-tubulin and Grip71, as well as Grip75, 128, or 163, are co-immunoprecipitated. **(B)**
1087 Mass spectrometry results from IPs with MBP-Cnn-T-N showing the presence of various γ-
1088 TuRC components. Note that Mzt1 is not expressed within embryos. Results of a control
1089 experiment on Grip75-GFP embryo extract not supplemented with any MBP-Cnn-T-N
1090 fragment are also shown. Numbers indicate emPAI scores as a proxy for protein abundance.
1091 Grip84 (A) and Grip84 (E) represent two different isoforms of Grip84 (promoters 1 and 2
1092 respectively).

1093

1094 **Figure S3**

1095 **Protein alignments of N-terminal regions of CM1 domain proteins.** **(A)** An alignment of
1096 Cnn-C homologues from different *Drosophila* species. The alignment was carried out in
1097 JalView keeping *D. melanogaster* at the top with the closest related species in order below.
1098 Only the N-terminal regions of the proteins were used in the alignment (~1-255aa). Potential
1099 phosphorylation patches are highlighted in yellow, with the proportion of S/T residues present
1100 in the *Drosophila melanogaster* sequence indicated in brackets. The CM1 domain is
1101 highlighted in purple. Red boxes and green arrows indicate α-helices and β-sheets based on
1102 predictions from JPred. **(B)** An alignment of the N-terminal region of Cnn-C with the equivalent

1103 N-terminal regions of its homologues in non-*Drosophila* species. Phosphorylation sites that
1104 promote binding to γ -TuRCs identified either in this study (*Drosophila* Cnn-C, T²⁷ and S¹⁸⁶) or
1105 other studies (*S. cerevisiae* S³⁶, S⁶⁰, T⁶⁴, T⁶⁸ and S⁹¹, *C. elegans* SPD-5, T¹⁷⁸, T¹⁹⁸; human
1106 CDK5RAP2, S¹⁴⁰) are indicated. Note that only the originally identified CM1 domain sequence
1107 (yellow) is conserved between homologues. The position of the “CM1 helix” (blue) and “CM1
1108 coiled coil (CC) region” (brown) recently identified in SPC110 are indicated, as is the γ -TuNA
1109 sequence from human CDK5RAP2 (green).

1110

1111 **Figure S4**

1112 **Polarity is established normally in pUbq-Cnn-C^T oocytes. (A-B)** Fluorescence images
1113 show localisation of Staufen protein in oocytes expressing pUbq-Cnn-C (A) or pUbq-Cnn-C^T
1114 (B) at stages 8, 9 and 10, as indicated. Staufen localised in the centre of the oocyte at stage
1115 8 and then at the posterior in stage 9 and 10 in all pUbq-Cnn-C (n=35, stage 8; n=35, stage
1116 9; n=30, stage 10) and all pUbq-Cnn-C^T (n=40, stage 8; n=50, stage 9; n=40, stage 10)
1117 oocytes that were imaged. **(C)** Fluorescence images show localisation of Gurken protein in
1118 oocytes expressing pUbq-Cnn-C or pUbq-Cnn-C^T at stage 9. Gurken protein was positioned
1119 close to the nucleus in the dorsal corner in all pUbq-Cnn-C (n=30) and all pUbq-Cnn-C^T (n=35)
1120 stage 9 oocytes. Gurken mis-positioning or its absence results in abnormal dorsal appendages
1121 that protrude from the surface of the egg, but the dorsal appendages were normal on all pUbq-
1122 Cnn-C (n=724) and all pUbq-Cnn-C^T (n=488) eggs.

1123

1124 **Figure S5**

1125 **Major spermatocyte defects are observed within testes from pUbq-Cnn-C^T flies**
1126 **(A,B)** Fluorescence images showing spermatocytes at different developmental stages (as
1127 indicated) from flies expressing either pUbq-Cnn-C (A) or pUbq-Cnn-C^T (B) fixed and stained
1128 for microtubules (green, α -tubulin), centrosomes (pink, Asterless), and DNA (blue). A high
1129 density of cytosolic microtubules, as well as cytokinesis and karyokinesis defects, are clearly
1130 observed in cells from pUbq-Cnn-C^T testes.

1131

1132 **Supplementary Videos**

1133 **Video 1**

1134 **Cnn-T scaffolds organise microtubule asters and can be mobile.** Movie showing Cnn-T
1135 scaffolds (green) organising microtubule asters (marked with Jupiter-mCherry (magenta)). A
1136 mobile scaffold (lower left) with an asymmetric microtubule aster can be seen moving through
1137 the cytosol.

1138

1139 **Video 2**

1140 **Transient spindle-like structures can form between Cnn scaffolds.** Movie showing the
1141 formation and disappearance of a transient spindle-like structure between adjacent Cnn-T
1142 scaffolds (green). Microtubules are marked with Jupiter-mCherry (magenta).

1143

1144 **Video 3**

1145 **Spindle-like structures organised by Cnn scaffolds can form in synchrony.** Movie
1146 showing the synchronous formation and disappearance of a multi-polar spindle-like array of
1147 microtubules that is subsequently organised by a nearby group of coalescing Cnn scaffolds
1148 (green). Microtubules are marked with Jupiter-mCherry (magenta)

1149

1150 **Video 4**

1151 **Microtubules are robustly anchored to Cnn scaffolds.** Movie showing rare giant Cnn-T
1152 scaffolds (green). One scaffold can be seen rotating and dragging the microtubules, indicating
1153 that the microtubules are robustly attached to the scaffold, presumably via γ -TuRCs.
1154 Microtubules are marked with Jupiter-mCherry (magenta).

1155

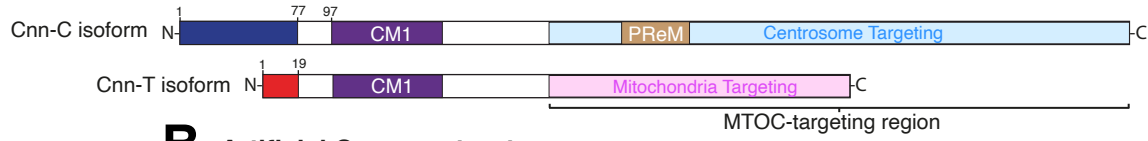
1156 **Video 5**

1157 **Expression of GFP-Cnn-T-N leads to the formation of dynamic microtubules within the**
1158 **cytosol of unfertilised eggs.** Video shows the effect of injecting mRNA encoding GFP-Cnn-
1159 T-N into unfertilised eggs expressing Jupiter-mCherry (marker of microtubules). Left panel
1160 shows the GFP channel (green), centre panel shows the RFP channel (magenta), right panel
1161 shows a merge.

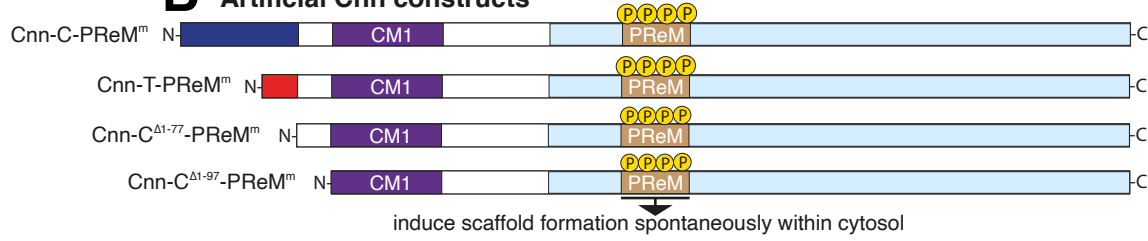
1162

Figure 1

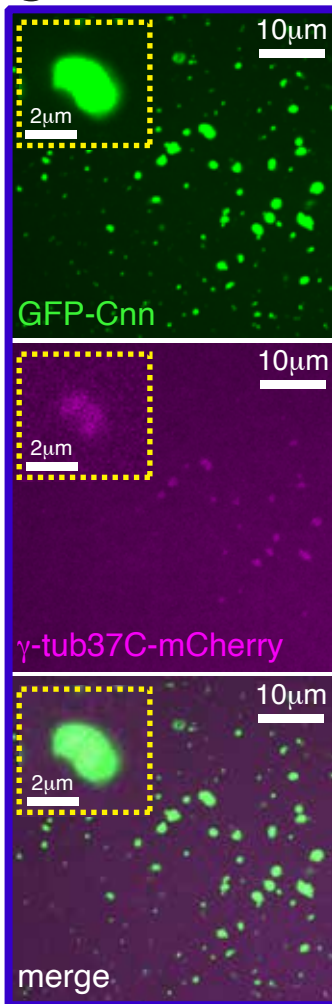
A True Cnn isoforms



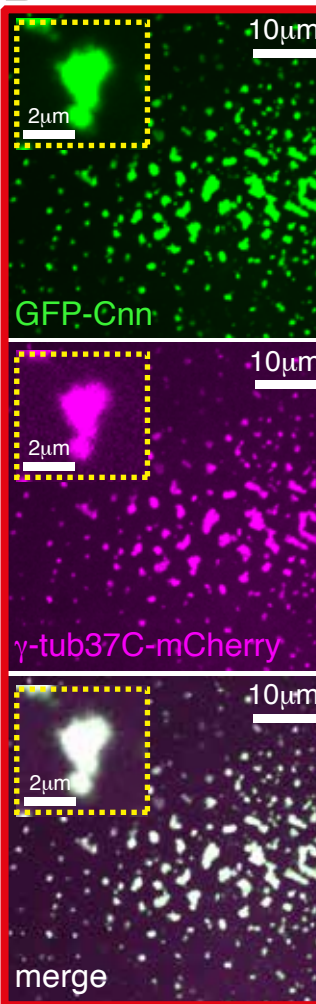
B Artificial Cnn constructs



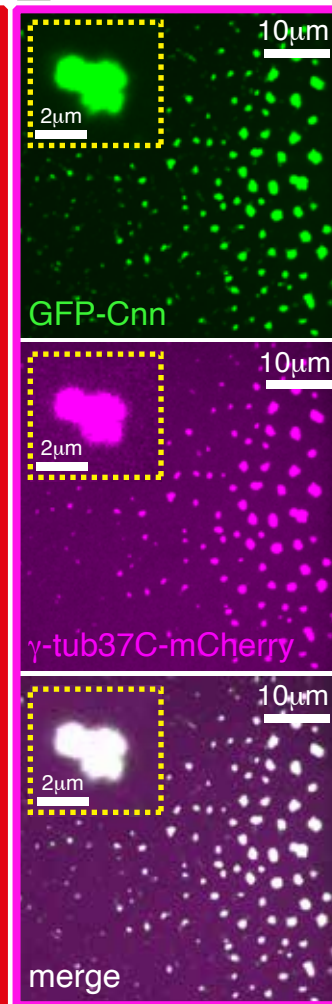
C Cnn-C scaffolds



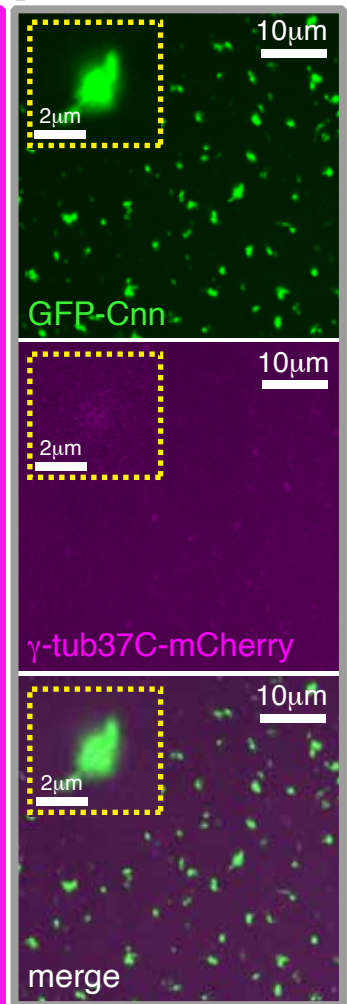
D Cnn-T scaffolds



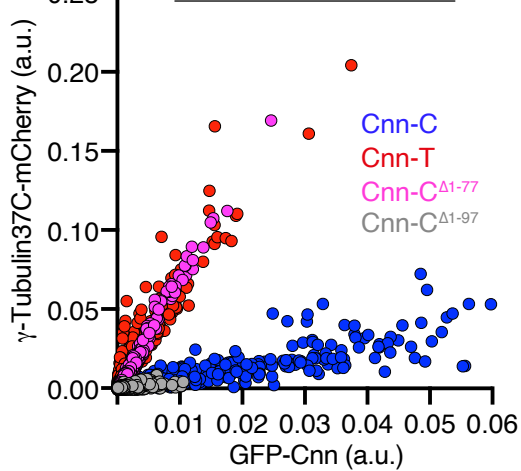
E Cnn-C^{Δ1-77} scaffolds



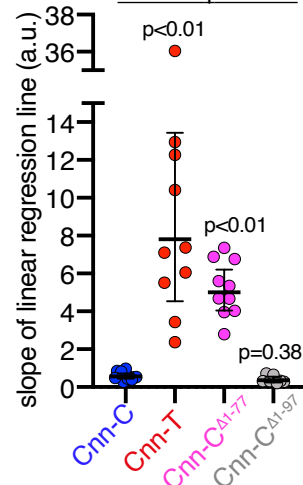
F Cnn-C^{Δ1-97} scaffolds



G individual scaffold values



H linear regression per egg Cnn vs γ-tubulin



I IP: MBP-Cnn-C-N MBP-Cnn-T-N MBP-Cnn-C^{Δ1-77}-N

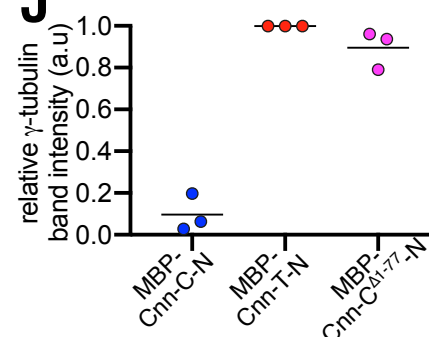
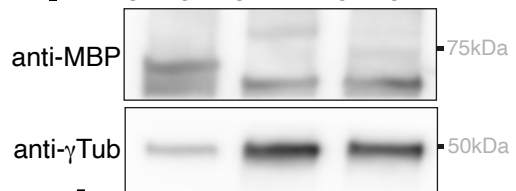


Figure 2

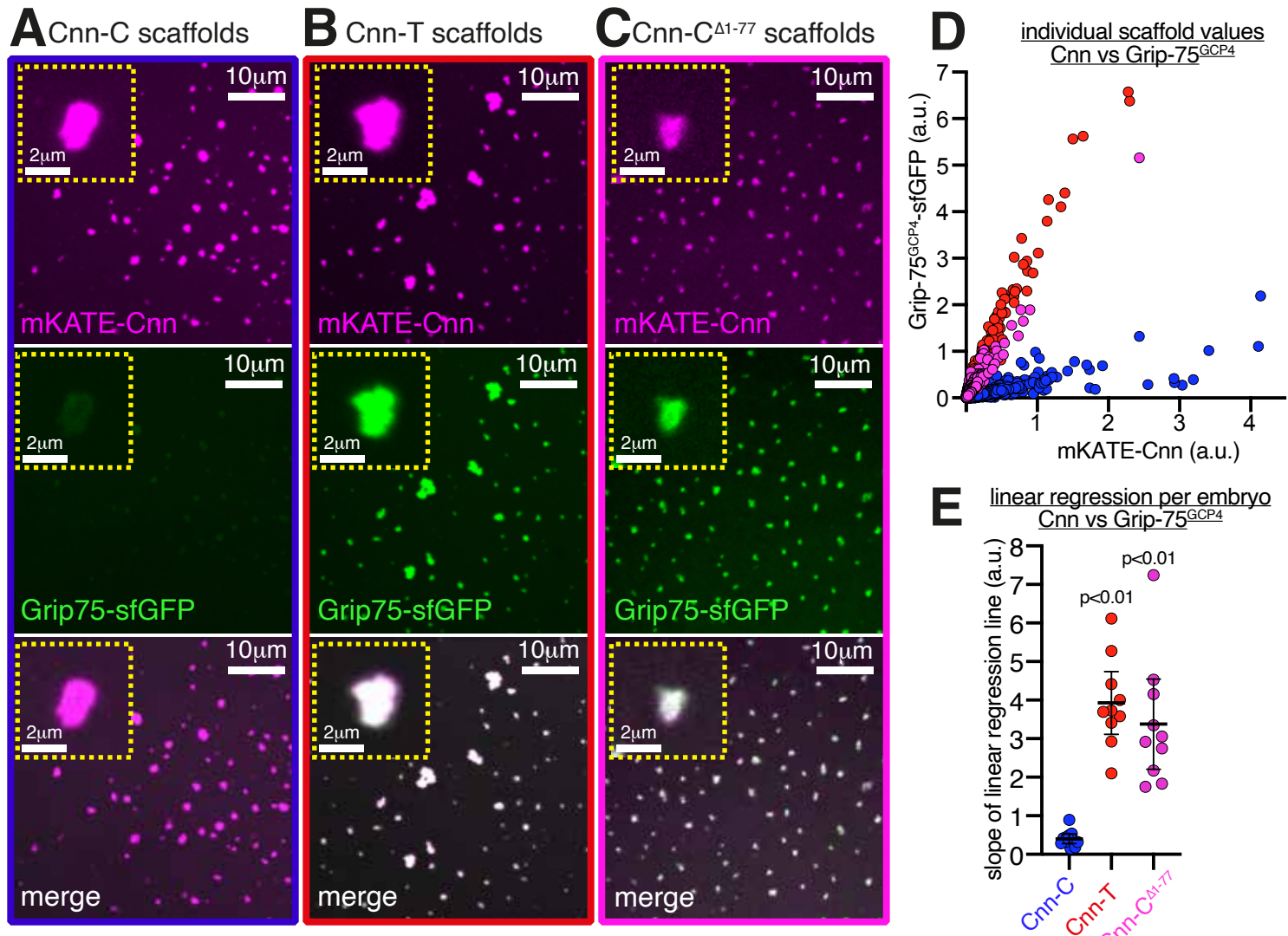


Figure 3

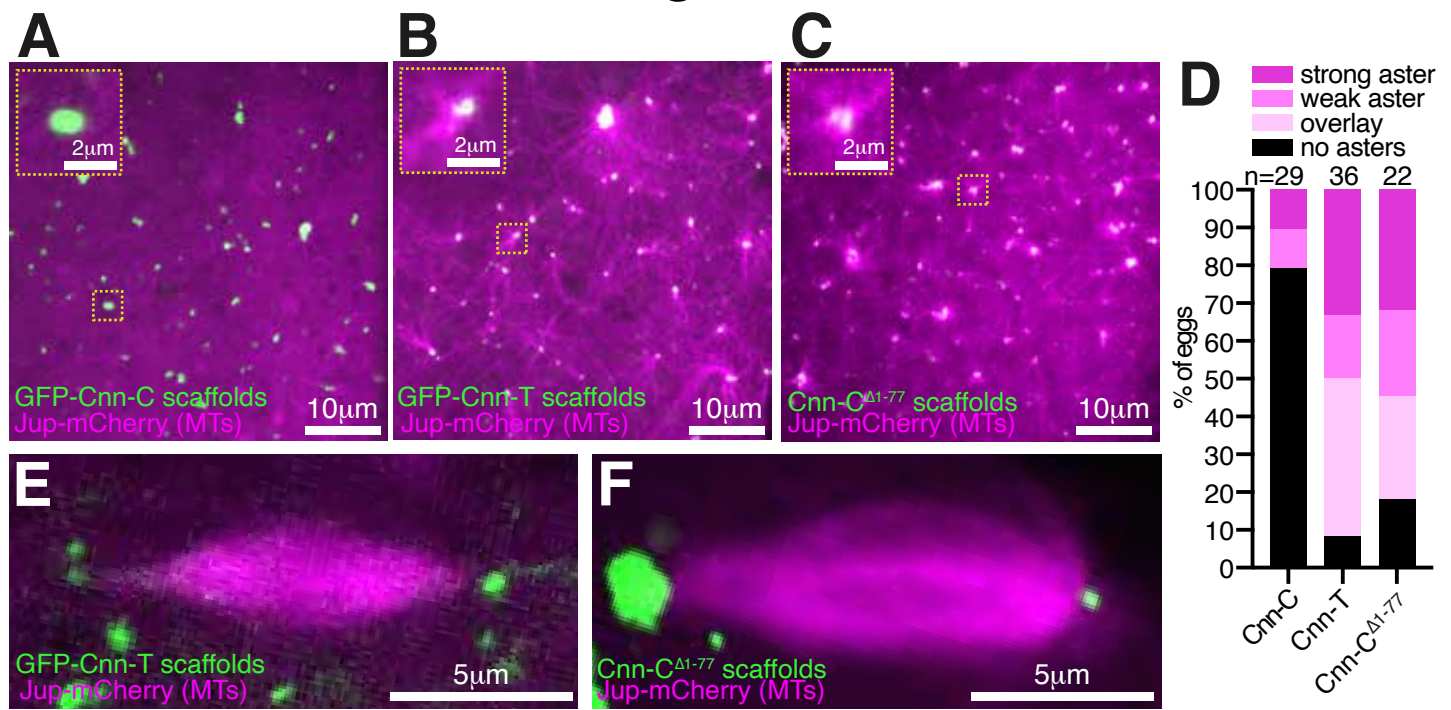
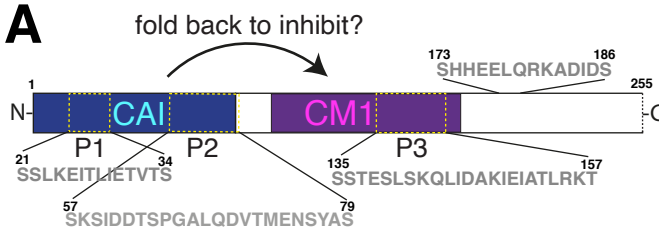
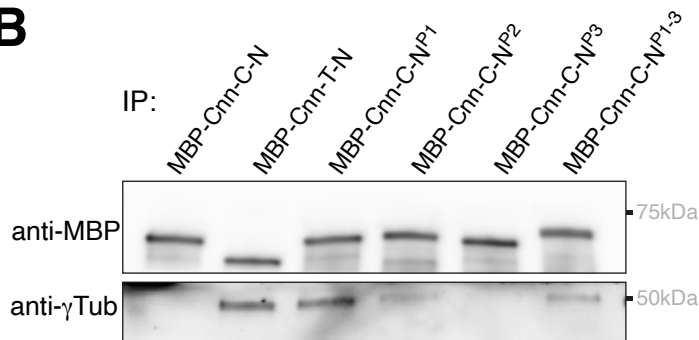


Figure 4

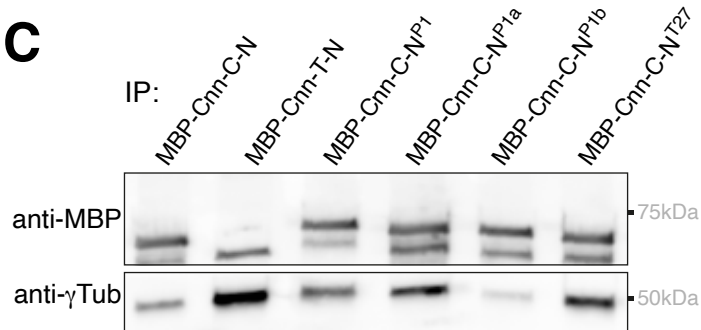
A



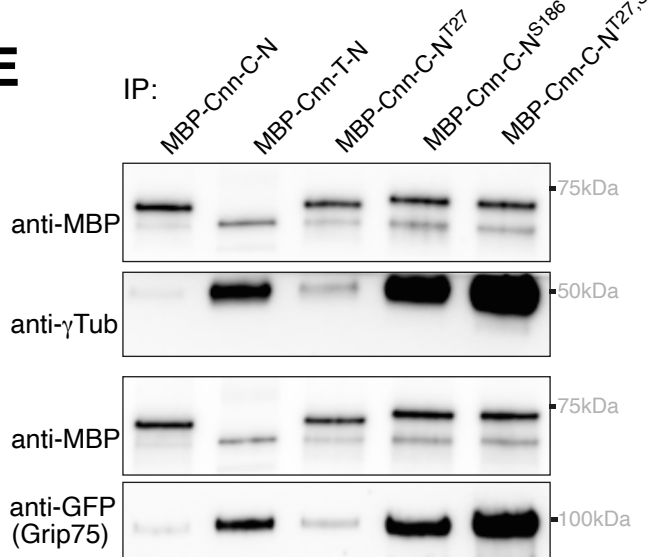
B



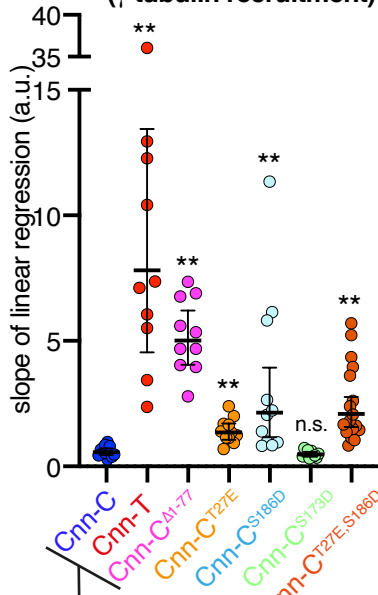
C



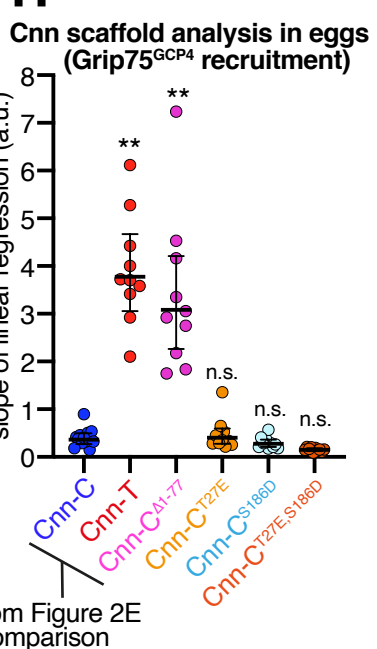
E



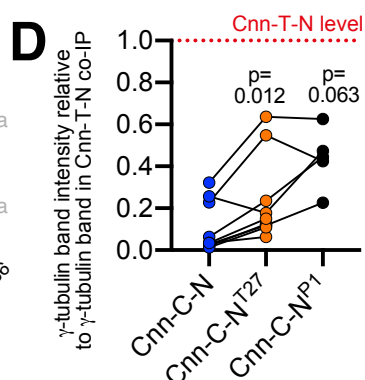
G Cnn scaffold analysis in eggs (γ -tubulin recruitment)



H



strong aster
weak aster
overlay
no asters



F

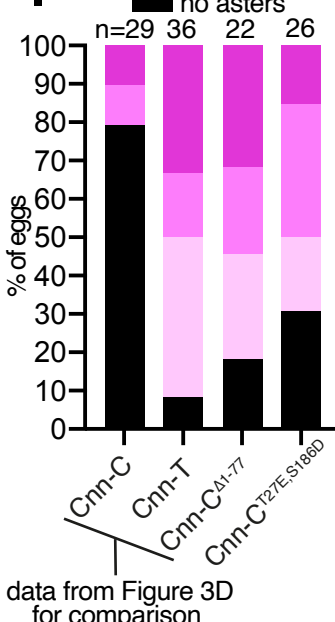
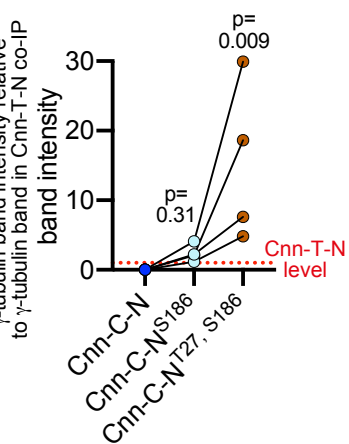


Figure 5

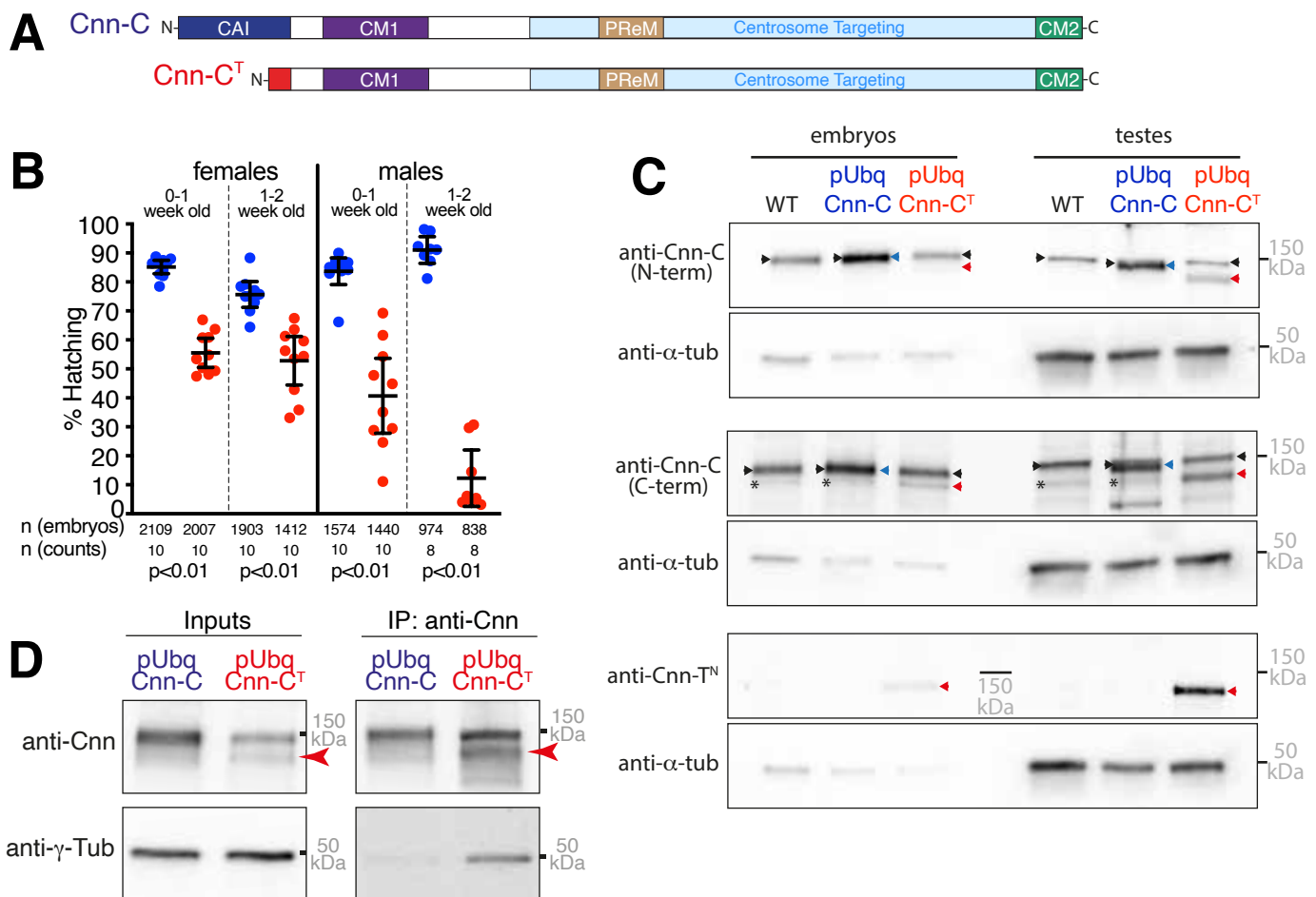
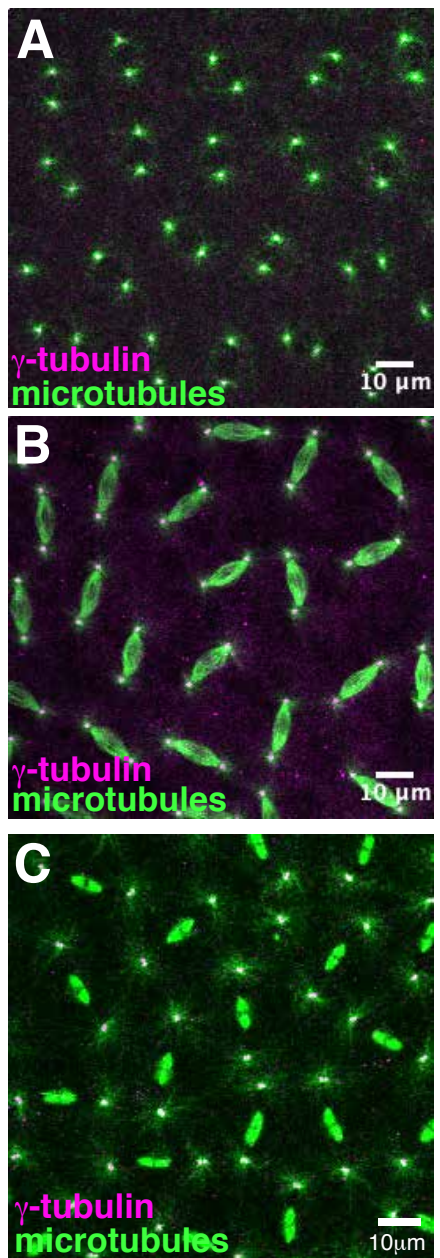
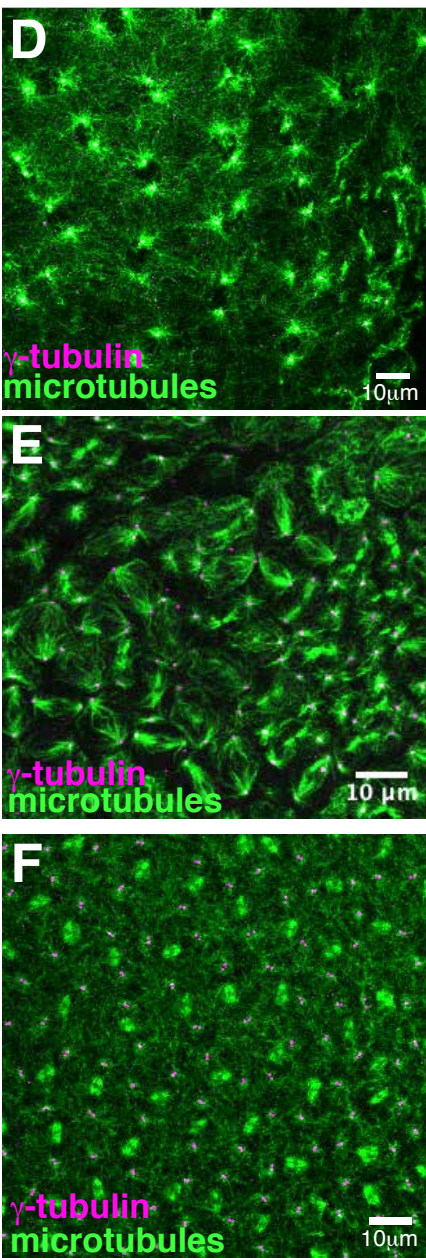


Figure 6

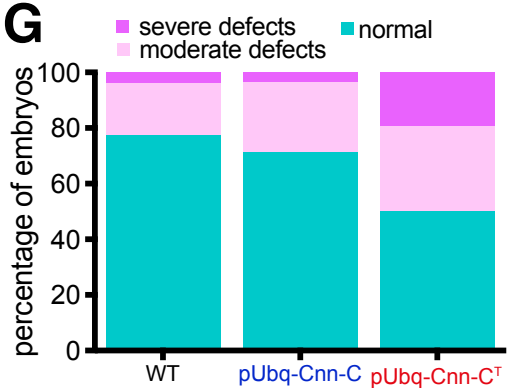
pUbq-Cnn-C



pUbq-Cnn-C^T



G



H

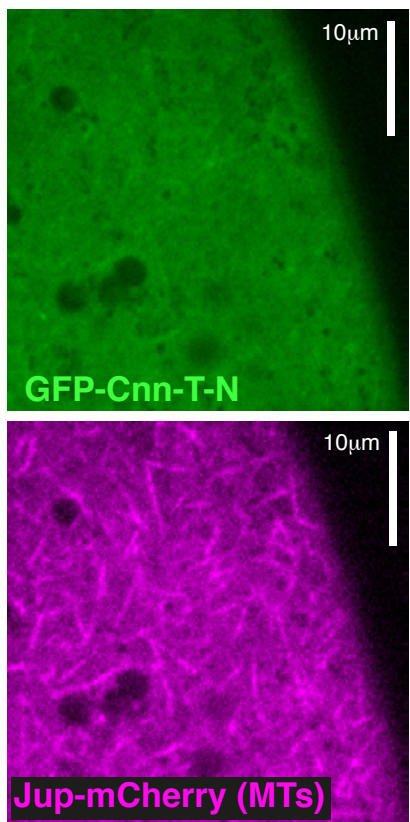


Figure 7

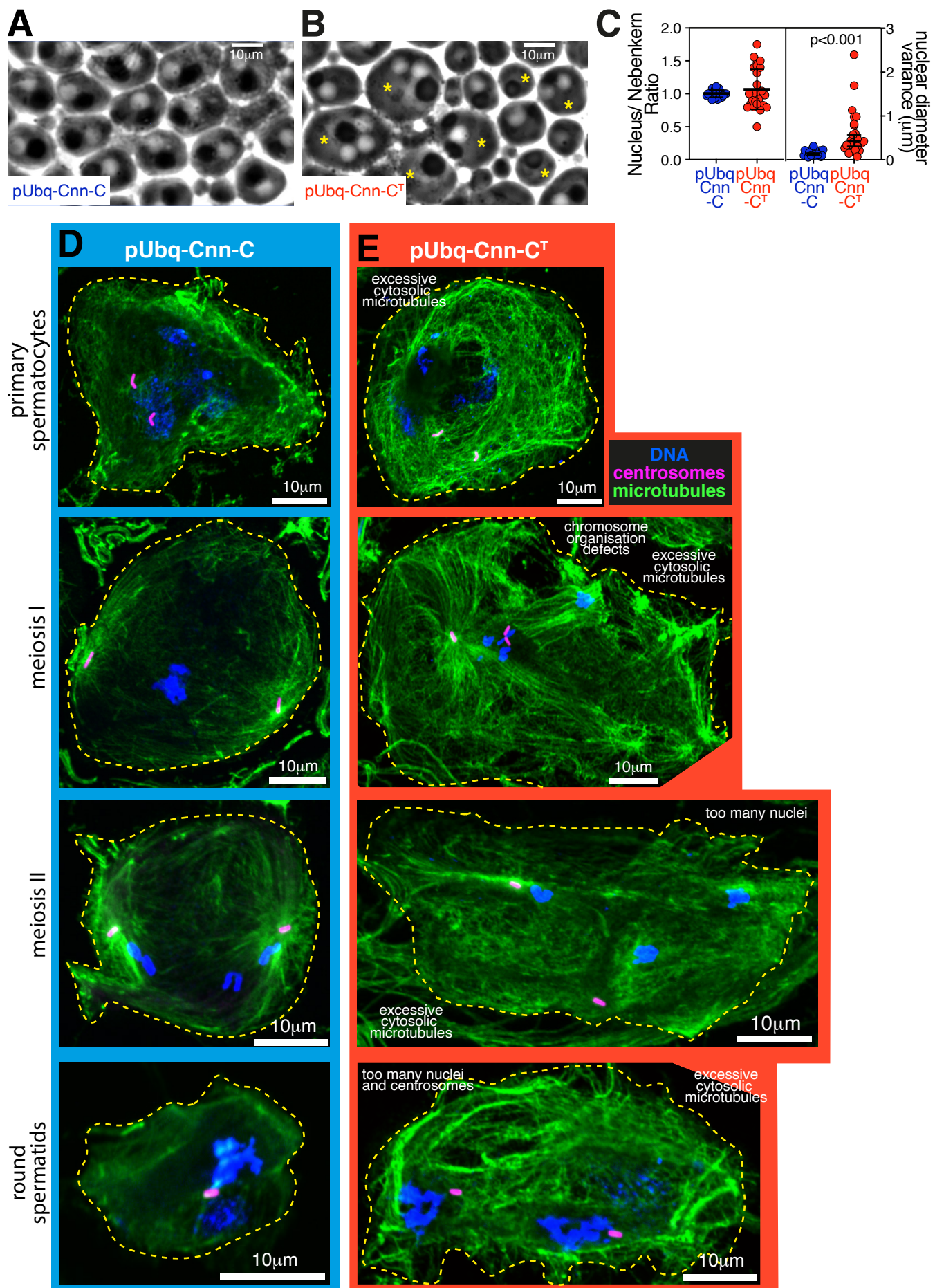
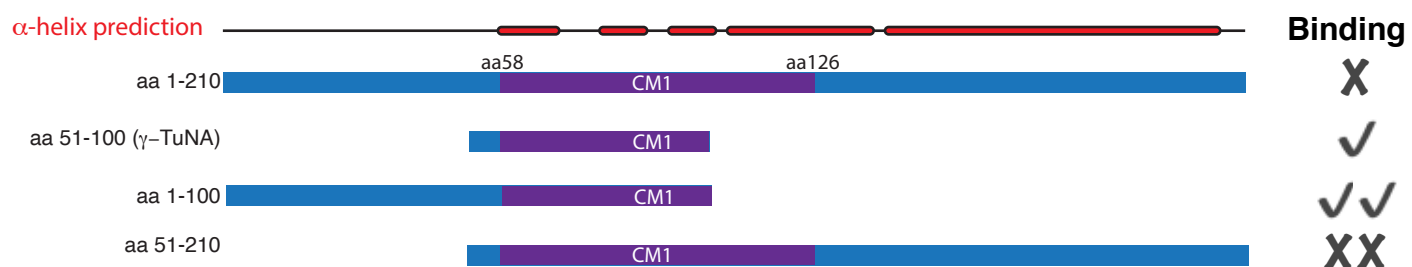
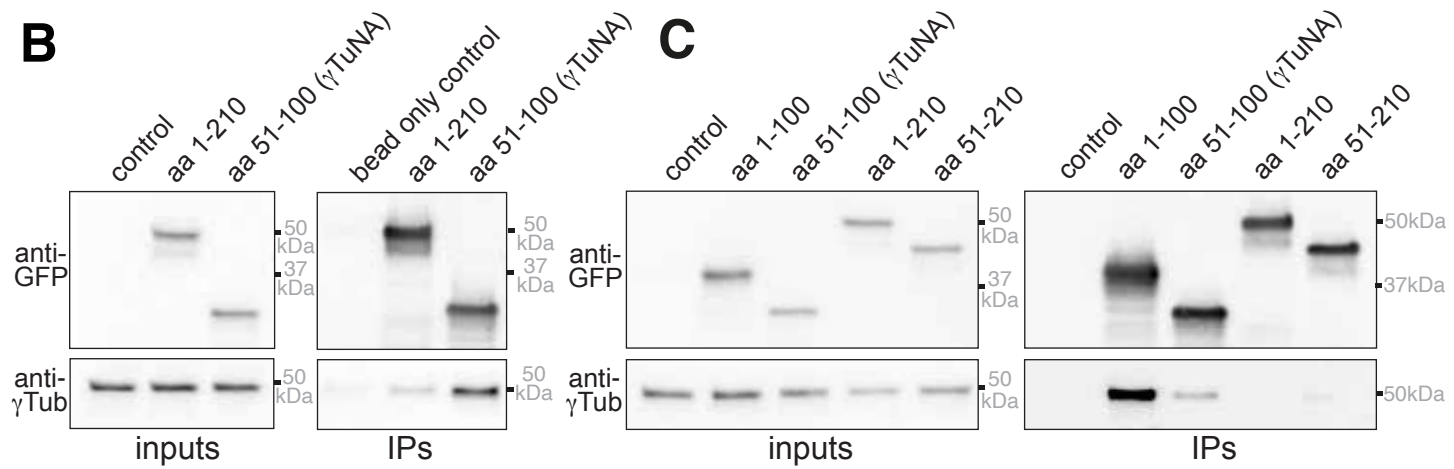


Figure 8

A



B



C

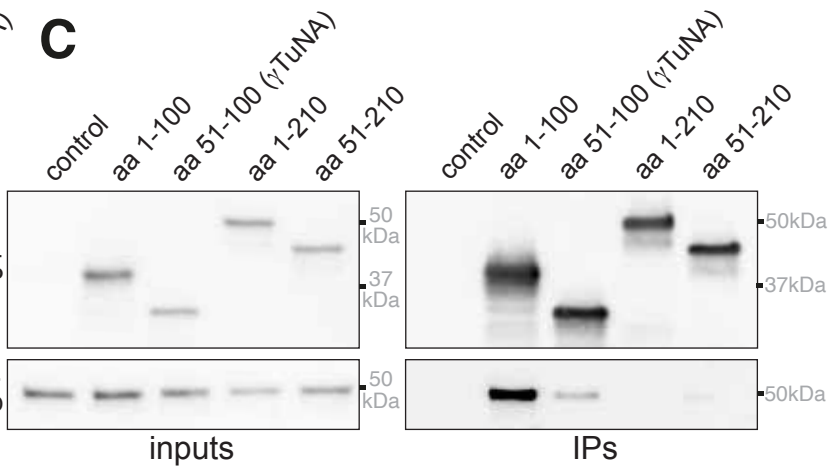
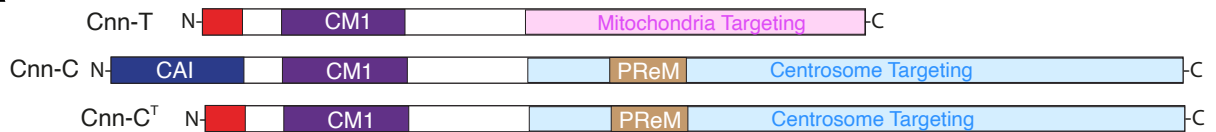
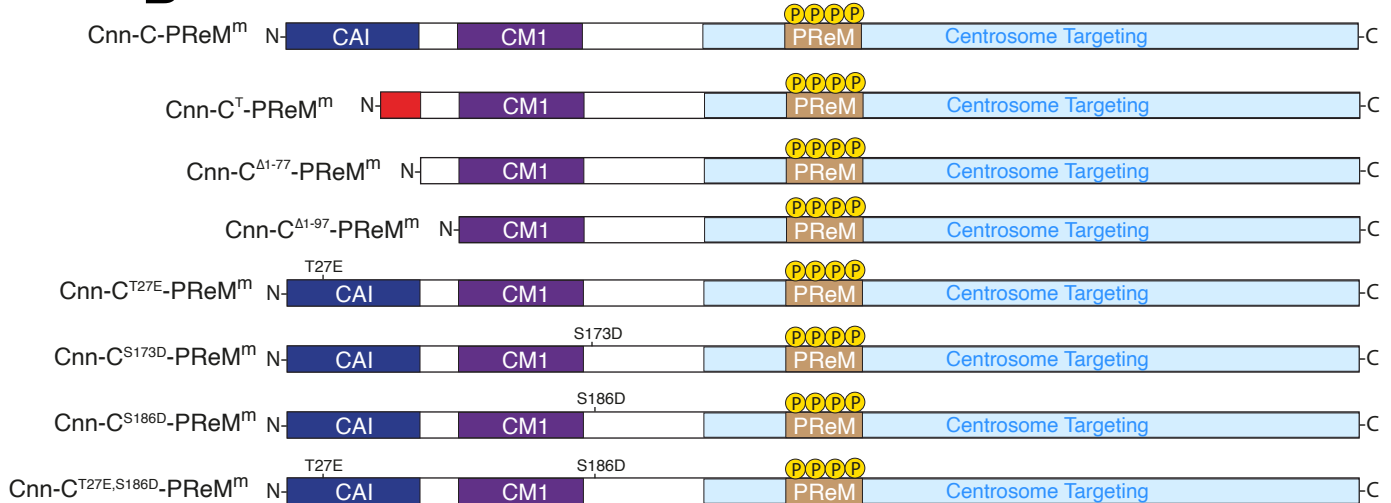


Figure S1

A



B



C

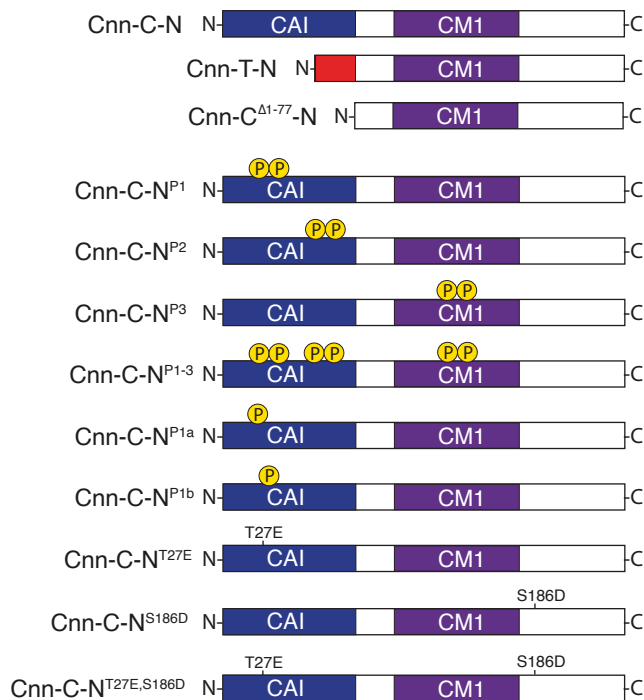
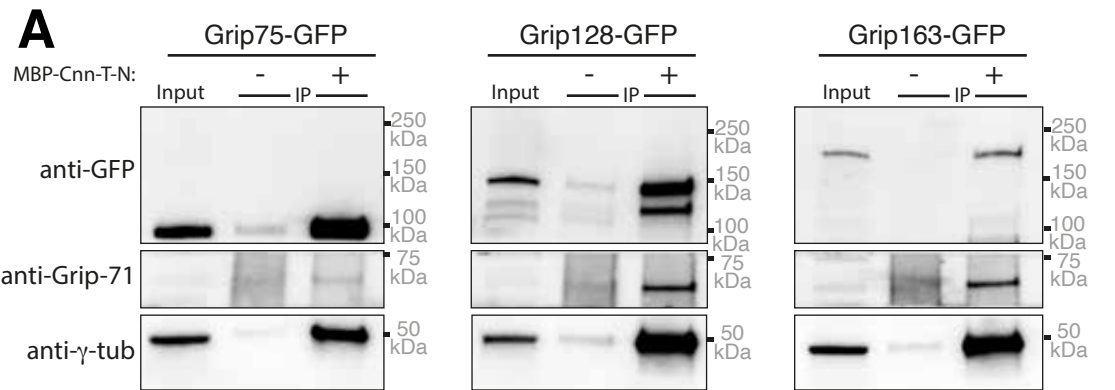


Figure S2

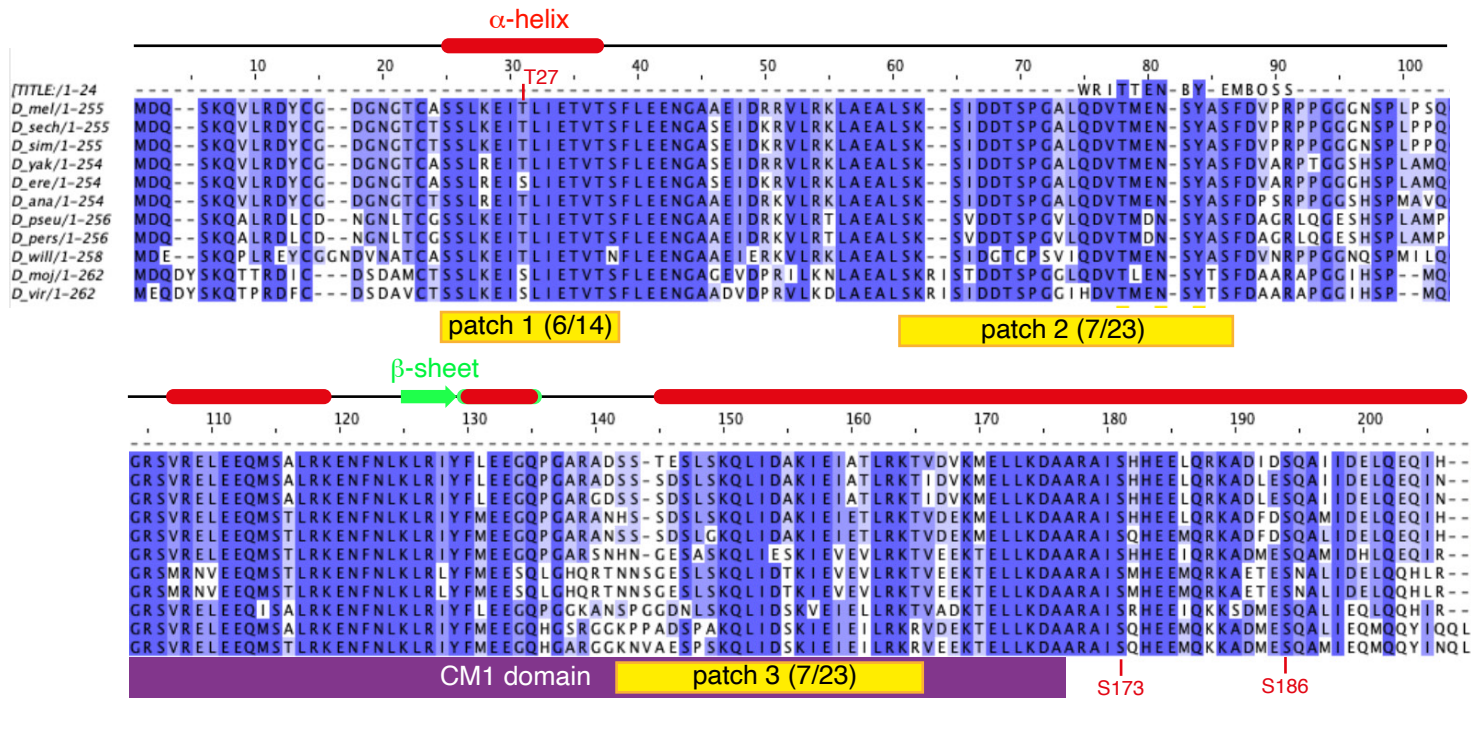


B

UniProt entry	Protein	G75, no fragment	G75 + Cnn-T-N	G128 + Cnn-T-N	G163 + Cnn-T-N
A0A0B4K6Z9	Cnn	-	4.50	15.63	13.03
M9PDN9	γ-tubulin 37C	0.45	24.45	63.16	39.41
P23257	γ-tubulin 23C	-	1.04	1.90	1.43
E1JJQ3	Grip84	-	1.76	8.14	4.76
Q8IQW7	Grip84	-	1.54	7.44	-
Q9XYP8	Grip91	-	1.74	4.45	3.54
Q9VKU7	Grip75	0.07	0.88	3.57	2.54
Q9VXU8	Grip128	-	0.08	0.40	0.16
Q9VTS3	Grip163	-	0.24	1.09	0.24
Q9VJ57	Grip71	-	0.30	1.87	0.93
x2JCP8	Actin	40.63	17.87	22.66	32.21

Figure S3

A alignment of Cnn-C N-terminal region between *Drosophila* species



B alignment of N-terminal region between species

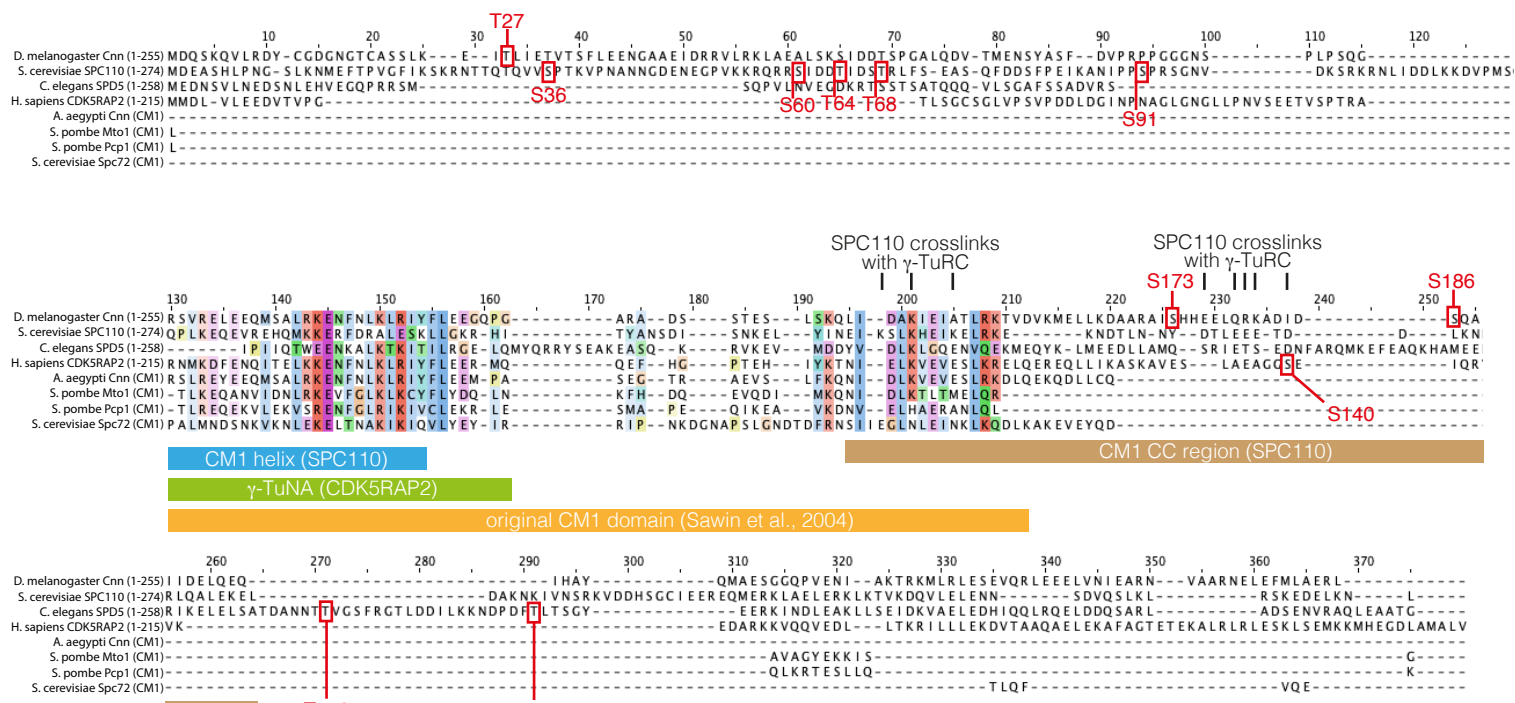


Figure S4

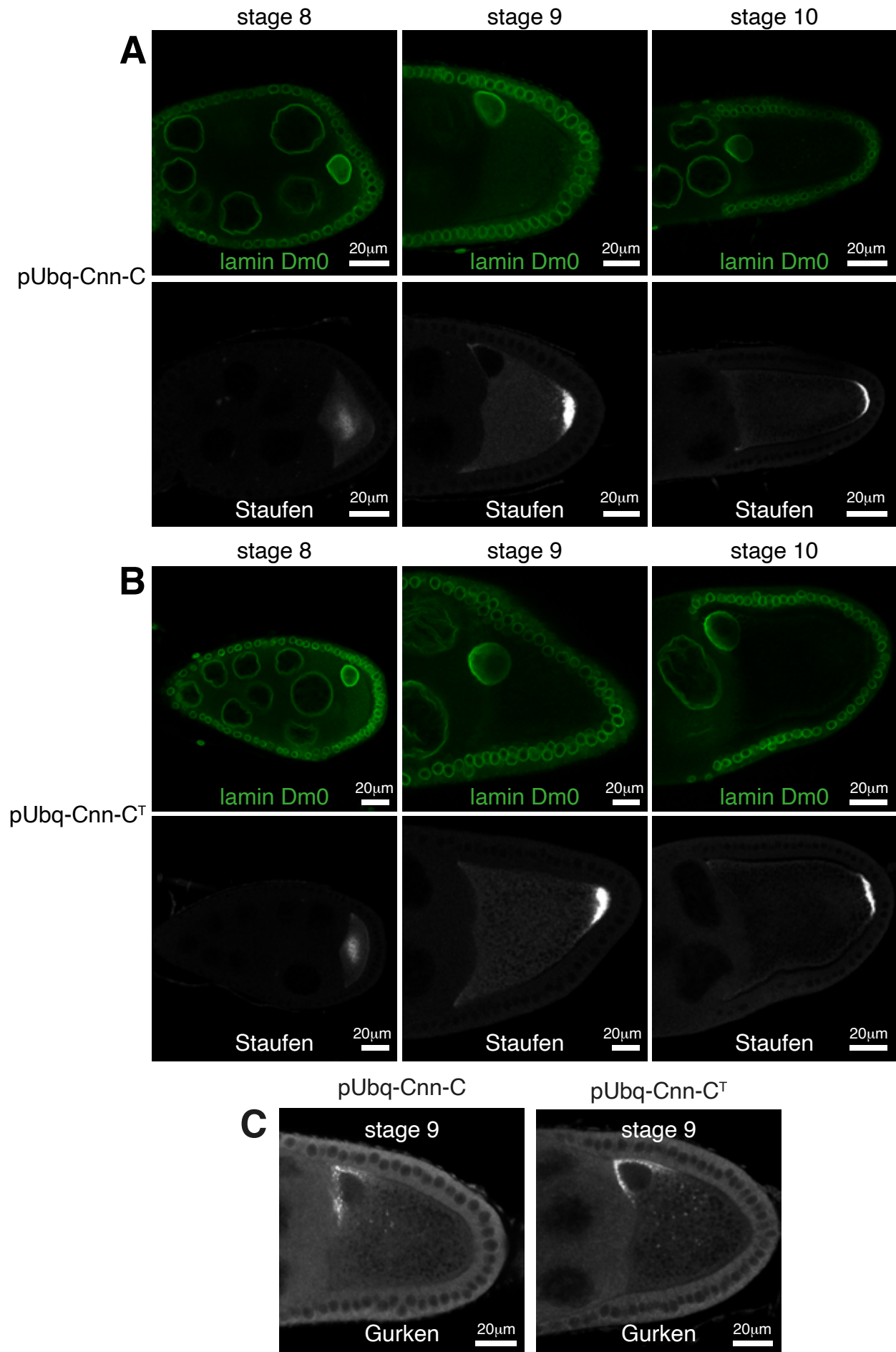


Figure S5

